THE JOURNAL OF PHYSICAL CHEMISTRY C
A JOURNAL OF THE AMERICAN CHEMICAL SOCIETY

pubs.acs.org/JPCC

Article

Band Gap Engineering toward Semimetallic Character of Quinone-Rich Polydopamine

Adrian Olejnik, Karol Olbryś, Jakub Karczewski, Jacek Ryl, Robert Bogdanowicz,* and Katarzyna Siuzdak

Cite This: *J. Phys. Chem. C* 2023, 127, 12662−12677

Read Online

ACCESS | Metrics & More | Article Recommendations | Supporting Information

ABSTRACT: Semiconductor|melanin interfaces have received increasingly more attention in the fields of photocatalysis and applied electrochemistry because of their facile synthesis, unique electrical properties, and strong capability toward photosensitization. In this work, we describe the electropolymerization of quinone-rich polydopamine (PDA) on the surface of hydrogenated TiO_2 nanotubes with enhanced photoactivity in the visible spectrum. PDA is deposited uniformly on the nanotube walls, and the chemical structures of the resulting PDA layer strongly depend on the pH of the supporting electrolyte. The film thickness varies in the range of 2−8 nm depending on the number of electropolymerization cycles. Optical and electrochemical experiments coupled with density functional theory simulations revealed strong evidence of a semimetallic character of the junction with a broad distribution of midgap surface states induced by PDA. As a result of the nanotube modification, a 20-fold increase in the photocurrent response is observed. Quantum efficiency measurements show that the enhancement occurs mainly at wavelengths between 500 and 550 nm. Additionally, nonlinear electrochemical impedance spectroscopy experiments strongly suggest that, in the TiO_2|PDA junction, PDA behaves as a set of redox mediators distributed at the surface rather than as a semiconducting polymer. This concept might be crucial for understanding the electronic properties of semiconductor|melanin junctions.

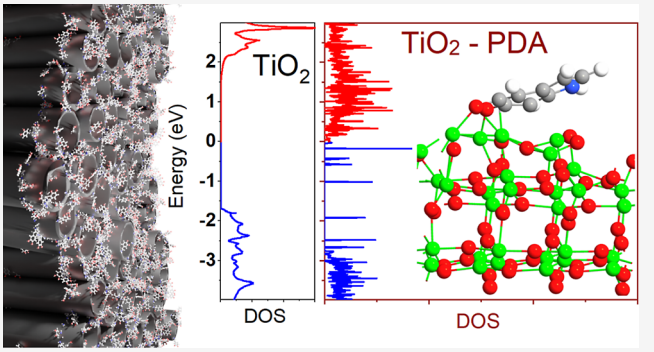

1. INTRODUCTION

Living organisms utilize melanins for several biological purposes, including pigmentation, adhesives, and as a building component of different tissues. Depending on the chemical structure and cellular functions, they can be divided into eumelanins, pyomelanins, pheomelanins, neuromelanins, and allomelanins.[1,2] The elucidation of the structure of melanin is generally a complicated issue and attracts significant attention among the community of chemists and material scientists.[3−5] A gold-standard synthetic eumelanin is polydopamine (PDA), which is a name for everything that is a product of oxidative polymerization of dopamine. The chemistry of PDA involves several tens of different structural units with many functional groups, such as catechol, quinone, indole, and amine. It is believed that the most abundant monomer of PDA is 5,6-dihydroxyindole (DHI) and its oxidized analogue indolequinone (IQ), which are double-ringed, π-conjugated molecules.[2,6−8] Additionally, some double-ringed units in the PDA chain can be hydrogen-saturated and thus not fully π-conjugated, such as leukodopaminechrome (LDC) and dopaminechrome (DC). It has also been shown that a minority of single-ringed units such as dopamine-quinone (DQ) and unchanged dopamine (DA) are also present in PDA.[6]

Although the presence of polymeric chains in PDA has been questioned for a long time, Delparastan et al. in 2018 used single-molecular force microscopy to provide direct evidence of the polymeric nature of PDA.[9] It is generally accepted that the structural units are connected by aryl−aryl linkages and covalent crosslinks. Moreover, hydrogen bonds and physical stacking of rings governed by $\pi-\pi$, π−cation, and electrostatic interactions also contribute to the structure.[6,8,10] The ratio between units of PDA and the degree of crosslinking can be controlled by the choice of deposition method, solvent, buffer pH, and other polymerization parameters.[2,3,11,12]

PDA has especially strong prospects due to its simplicity of polymerization onto practically any surface and the high malleability of its electrical and optical properties through manipulation of energy levels in the π-conjugated systems.[3,13] The presence of redox active sites involving catechol/quinone pairs in PDA can be utilized in many areas of electrochemistry, such as supercapacitors,[14] catalysis,[15] and probes in chemical force microscopies.[16] Due to the wide variety of intermolecular

Received: December 16, 2022
Revised: June 7, 2023
Published: June 24, 2023

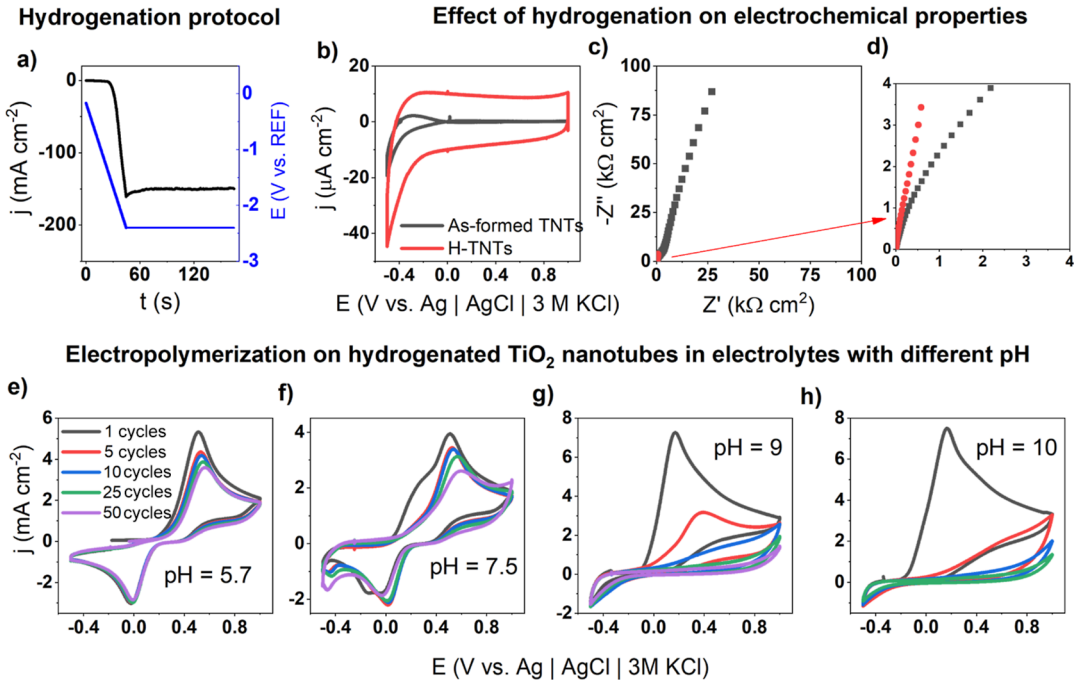

Figure 1. Hydrogenation of TNTs and electropolymerization of dopamine. (a) Potential program and current response of nanotubes during hydrogenation; (b–d) CV curves and EIS spectra of as-prepared and hydrogenated nanotubes (supporting electrolyte: 0.5 M Na_2SO_4); (e–h) CV curves registered during electropolymerization with 5 mM dopamine in electrolytes of different pH of 5.7, 7.5, 9.0, and 10.0 (supporting electrolyte: 1× Tris +0.5 M Na_2SO_4).

interactions, PDA is known as a prominent adhesive and as a binder for many composite materials.[3] Moreover, it is composed only of highly abundant nonmetal atoms, which is beneficial for sustainable, green chemistry solutions.[4] However, in recent years, researchers have focused on further expansions of the variety of these structures by introducing new monomers,[1] with copolymerization agents[17,18] or as a template for molecular imprinting of biomolecules.[19]

The molecular mechanisms underlying the electronic properties of melanins, including PDA, are complicated and not fully understood yet. Traditionally, eumelanins were considered amorphous semiconductors due to the characteristic dependence of the conductivity on temperature.[12,20] However, Mostert et al. showed in 2012 that this view is incorrect.[21] Based on EPR measurements, they showed that the comproportionation reactions—especially in DHI carboxylic acid (DHI-CA) units—lead to the creation of protons and hydroxyl ion radicals as ionic charge carriers. In addition to polaronic-based charge transport in π-conjugated systems, there is also a strong component of ionic conduction. Furthermore, in a thorough study using picosecond/femtosecond fluorescence spectroscopy, PDA structural units were shown to differ in terms of the capability of proton transfer.[22] For example, the rates of these processes are up to 1000 times slower for DHI compared to its carboxylated analogue, which explains the higher conductivity of DHI-CA.

In addition to the electronic properties of PDA itself, an area actively exploited nowadays is PDA|semiconductor junctions. Kim et al. explored the PDA|ZnS interface using photoelectrochemical experiments and density functional theory (DFT).[23] In that study, it was shown that, after PDA deposition, some ZnS surface regions are oxidized to ZnSO, leading to changes in the local band structure. As a result, a doubly staggered band alignment is created. On the one hand, ZnSO lowers the band gap and the capability of trapping photoexcited electrons for catalysis; on the other hand, PDA can accept holes from the valence band (VB) and thus prevent photocorrosion (acting as a reversible hole scavenger). A similar effect was observed a decade earlier in EPR studies by Dimitrijevic et al. on the TiO_2|PDA interface.[24] They showed the localization of holes on PDA, which prevents the oxidation of water and the creation of free radicals. At the same time, however, dopamine did not affect the reductive ability of photogenerated electrons in the TiO_2 conduction band. In other words, the recombination of holes with electrons is suppressed because of the unique staggered band alignment.

Guan et al. reported that PDA can also be used as a binder integrating multicomponent sulfides on TiO_2 nanowires.[25] They showed that the thickness of the PDA layer is a crucial factor in determining the magnitude of the boost in photoactivity and electrochemical properties. Specifically, 1 nm-thick PDA is too thin to efficiently enhance absorption, while 3 nm produces optimal photosensitization. However, layers thicker than 3 nm impede the charge transfer kinetics by shielding active sites, thus limiting the electrochemical performance, presumably due to the longer distance for the charge carrier tunneling. In another work, core–shell TiO_2 @PDA nanoparticles exhibited the highest photocatalytic enhancement with 1 nm-thick PDA.[26] These investigations suggest that the optimal thickness for photosensitization is strongly dependent on the geometry of the substrate material.

In this work, we report on experimental and computational investigations of the electronic structure of PDA and report for the first time a semimetallic character of the PDA|semiconductor interface. Both experiments and DFT calculations of the density of states (DOS) show that quinone-rich, electropolymerized PDA exhibits highly populated midgap states and a high propensity toward photosensitization. When deposited on

https://doi.org/10.1021/acs.jpcc.2c08804
J. Phys. Chem. C 2023, 127, 12662–12677

hydrogenated loosely spaced titania nanotubes (TNTs), it results in a 2000% enhancement of photocurrents, mainly in the visible spectrum after PDA modification as well as unique electrochemical behavior in the presence of ferrocyanides. Based on these observations, we propose a model in which PDA is treated as a set of distributed redox mediators, rather than as an organic semiconductor, with high explanatory power for other interfaces involving PDA.

2. MATERIALS AND METHODS

2.1. Reagents. 10× Tris buffer was obtained from Santa Cruz Biotechnology and diluted 10 times prior to the measurements, dopamine hydrochloride was purchased from Sigma-Aldrich, and the deionized water used in the experiment was provided by a Hydrolab HLP-5p system. A titanium plate (99.7% purity) was obtained from Strem Chemicals. Na_2SO_4, acetone, ethanol, diethylene glycol, HCl, NaOH, $K_3[Fe(CN)_6]$, $K_4[Fe(CN)_6]$, and NH_4F were provided by Chempur.

2.2. Synthesis of Loosely Spaced TNTs. The titania nanotube synthesis was reported previously elsewhere.[27,28] Prior to anodization, the titanium plate was ultrasonically cleaned in acetone, ethanol, and subsequently water. Single-step anodization of the titanium plate was performed in an electrolyte containing diethylene glycol/water/HF (69/5/1 vol %) and 9.4 mM NH_4F. The anodization voltage was 30 or 40 V (as indicated in the text), the polarization time was 2 h, and the temperature was 40 °C. After anodization, the TNTs were rinsed with ethanol and dried in an air stream. Finally, the plates were calcined in a tube furnace (Nabertherm) at 450 °C for 2 h.

2.3. Hydrogenation of TiO_2 Nanotubes and Electropolymerization of Dopamine. All electrochemical experiments, including the hydrogenation and electropolymerization of dopamine, were performed using a Biologic SP-150 potentiostat−galvanostat. Unless stated otherwise, the working electrode was hydrogenated pure or modified TNTs, the counter electrode was a platinum mesh, and the reference electrode was AglAgCll3 M KCl. All potentials in the study are expressed with respect to this reference electrode. The geometric surface areas of the working electrodes were between 0.5 and 1 mm^2, and all currents were transformed to current densities.

Hydrogenation of TNTs was performed in an argon-purged 0.5 M Na_2SO_4 solution through the following protocol. First, linear sweep voltammetry (LSV) with a 100 mV/s rate was used for cathodic polarization up to −2.4 V. Then, a constant potential equal to −2.4 V was applied for 2 min (Figure 1a).

Electropolymerization of dopamine on hydrogenated TNT electrodes was carried out potentiodynamically in an argon-purged solution of 0.5 M Na_2SO_4 containing 1× Tris buffer, immediately after hydrogenation. The pH of the solution was adjusted by adding 1 M HCl or 1 M NaOH to the desired values, i.e., 5.7, 7.5, 8.5, 9.0, or 10.0. An MP-103 handheld potentiometric pH meter was used to control the pH value. The number of cyclic voltammetry (CV) cycles was 5, 10, 25, or 50 with a 20 mV/s scan rate in the range from −0.5 to +1.0 V.

2.4. SEM Inspection and Measurement of the PDA Film Thickness. The surface morphology of the electrodes was investigated by means of a Quanta FEG 250 (FEI) Schottky field-emission scanning electron microscope equipped with a secondary ET electron detector with a beam accelerating voltage of 10 kV. The thickness of the PDA layer (d_{PDA}) was estimated by measuring the wall thickness of the PDA-modified nanotubes ($W_{TNT|PDA}$), subtracting the thickness of the unmodified nanotubes (W_{TNT}), and then dividing it by 2 (eq 1)

$$d_{PDA} = \frac{W_{TNT|\,PDA} - W_{TNT}}{2} \quad (1)$$

Measured values were averaged over at least 100 points.

2.5. X-ray Photoelectron Spectroscopy. X-ray photoelectron spectroscopy (XPS) studies were carried out on an ESCALAB 250Xi multispectroscope (Thermo Fisher Scientific) operating with an Al Kα X-ray source. The spot size was 650 μm, and the pass energy through the hemispherical analyzer was 20 eV. Throughout the measurement, the samples were flooded with low-energy electrons and low-energy Ar^+ ions to assure charge compensation, with a final peak calibration at adventitious carbon C 1s (284.8 eV). The obtained spectra were analyzed and deconvoluted using the Avantage v5.9921 software (Thermo Fisher Scientific).

2.6. Diffuse Reflectance, UV + Vis, and Raman Spectroscopy. Diffuse reflectance spectra were collected with a PerkinElmer Lambda 35 (PerkinElmer, Waltham, MA, USA) dual-beam spectrophotometer in the range of 200−1000 nm with a scanning speed of 60 nm/min.

The Kubelka−Munk (KM) functions $F(R)$ were calculated on the reflectance R data according to eq 2[29]

$$F(R) = \frac{(1-R)^2}{2R} \quad (2)$$

Raman spectroscopy measurements were conducted using a confocal micro-Raman spectrometer (inVia, Renishaw, Wotton-under-Edge, Gloucestershire, UK) with an argon-ion laser source emitting at 514 nm and operating with a power of 10 mW.

2.7. Incident Photon Conversion Efficiency. Quantum efficiency maps were measured with a photoelectric spectrometer for quantum efficiency measurements (Instytut Fotonowy, Poland). The wavelength range was set from 600 to 200 nm, and a measurement point was taken every 25 nm. The photoresponse regarding the wavelength was recorded in the potential range between −200 and 1000 mV, and the spacing between points was 200 mV. The illumination source was calibrated using a silicon reference cell.

2.8. Electrochemical and Photoelectrochemical Characterization. The effects of hydrogenation on the properties of TNTs were verified in a 0.5 M Na_2SO_4 electrolyte with CV with a 50 mV/s scan rate, as well as electrochemical impedance spectroscopy (EIS) at open circuit potential and a 10 mV amplitude of stimulating single-sine potential waves. The frequency range for this experiment was 100 kHz−100 mHz (96 points per decade), and the electrode was preconditioned for 3 min before EIS measurement to preserve equilibrium.

Photoelectrochemical tests were performed in a 0.5 M Na_2SO_4 electrolyte using LSV with a scan rate of 20 mV/s or using chronoamperometry (CA) at a potential of +0.3 V. As a light source, a xenon lamp equipped with AM 1.5 and UV cutoff (GG40, Schott) filters was used. The irradiation intensity was established to be 100 mW/cm^2 using a Si reference cell (Rera). The EIS measurements used for Mott−Schottky were performed at potentials ranging from −0.5 to +1.0 V with a 1 min polarization time at each step and a 10 mV sine amplitude. The inverse squared capacitance was calculated from the impedance data at a 1 kHz frequency.

https://doi.org/10.1021/acs.jpcc.2c08804
J. Phys. Chem. C 2023, 127, 12662−12677

Scheme 1. Experimental Procedure to Obtain Loosely Spaced TNT Covered with PDA

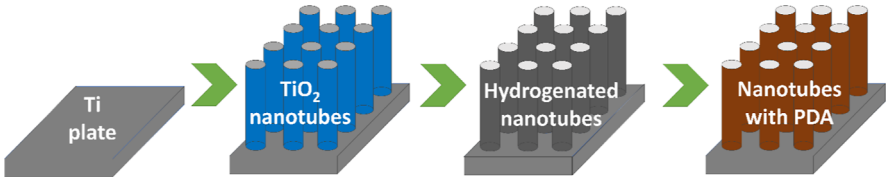

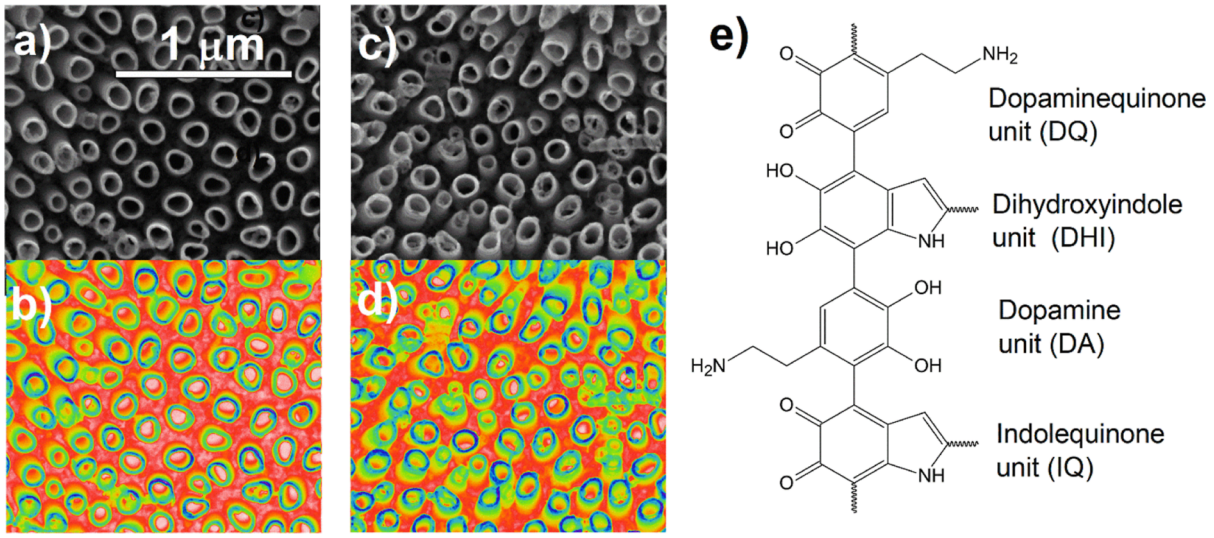

Figure 2. SEM images with different color contrasts of (a–b) pure nanotubes and (c–d) nanotubes with deposited PDA at pH = 7.5; (e) fragments of the molecular structure of PDA.

The semimetallic properties of the TNT|PDA junction were established by CV and EIS experiments in an electrolyte containing 5 mM $K_4[Fe(CN)_6]$ and 5 mM $K_3[Fe(CN)_6]$ with a 1 M KCl supporting electrolyte. Prior to each EIS measurement, the working electrode was polarized to +0.260 V for 1 min. The amplitudes of the voltage stimulus were 10, 100, 200, 300, or 500 mV, and the frequency range was 100 kHz–100 mHz.

2.9. DFT Computations. Molecular structures of anatase surfaces and PDA units were designed using a builder tool provided by Atomistix ToolKit Quantumwise (ATK, Synopsys, USA) as reported in ref 30. DFT computations were performed using the Perdew–Burke–Ernzerhof (PBE) functional within the generalized gradient approximation implemented in the package. The linear combination of the atomic orbital method[31] with the medium ATK basis set and PseudoDojo norm-conserving pseudopotentials were applied.[32] The adsorption geometry and intermolecular interactions between dopamine structural units and TiO_2 were investigated by geometry optimizations and calculating electron density maps in optimized structures. A preoptimization using a Dreiding force field was used to facilitate several geometry optimizations.[33] The DOS was calculated with a 7 × 7 × 1 A^3 *k*-point mesh and a density mesh cutoff of 125 Ha and using half-occupation (DFT—1/2) correction.[34] The DOS spectra of isolated monomers, dimers, and trimers of PDA were computed for the optimized structures using multipole boundary conditions (single *k*-point). Adsorption simulations were performed using slab models of anatase TiO_2 cleaved along the (101) crystallographic plane of an anatase unit cell and containing 30 atoms of Ti each (5 layers of Ti atoms). This plane was chosen because it is one of the most abundant planes in the experimental XRD spectrum and electron diffraction pattern.[35,36] The symmetry-reduced body-centered tetragonal unit cell of anatase used for preparing the slab was taken from the Quantum ATK database, having a size of 3.79 × 3.79 × 9.51 Å. The final supercell used for adsorption models throughout the paper was 11.35 × 10.23 × 36.09 Å with 28 Å of vacuum. Prior to adsorption, the molecule of the PDA monomer/dimer/trimer was placed 5 Å above the surface and relaxed. DOS spectra were calculated based on Kohn–Sham orbitals calculated for the last frame of geometry optimization.

3. RESULTS AND DISCUSSION

3.1. Hydrogenation of TNTs and Electropolymerization of Dopamine. The overall synthetic procedure is shown in Scheme 1. Prior to enhancement of the surface conductivity, TNTs were electrochemically hydrogenated according to the protocol depicted in Figure 1a. This process has been shown to lead to the incorporation of hydrogen atoms into the surface layer of TiO_2 unit cells, introducing several energy levels within the energy gap and increasing the electronic populations inside the conduction band.[37−39] As a result, a significant increase in capacitive currents is observed in both the cathodic and the anodic branches (Figure 1b). Moreover, the real and imaginary parts of the impedance are significantly decreased (Figure 1c,d), indicating an enhancement of both the surface conductivity of the nanotubes and template and the double-layer capacitance.

Subsequently, the hydrogenated nanotubes were subjected to electropolymerization of dopamine in a 0.5 M Na_2SO_4 electrolyte buffered with 1× Tris and the pH adjusted to different levels, i.e., 5.7, 7.5, 9.0, and 10.0. Due to the fact that the electrochemical steps of PDA electropolymerization are proton-coupled[40] and the chemical steps are base-catalyzed,[7,41] significant pH dependence of the PDA structure and properties

https://doi.org/10.1021/acs.jpcc.2c08804
J. Phys. Chem. C 2023, 127, 12662−12677

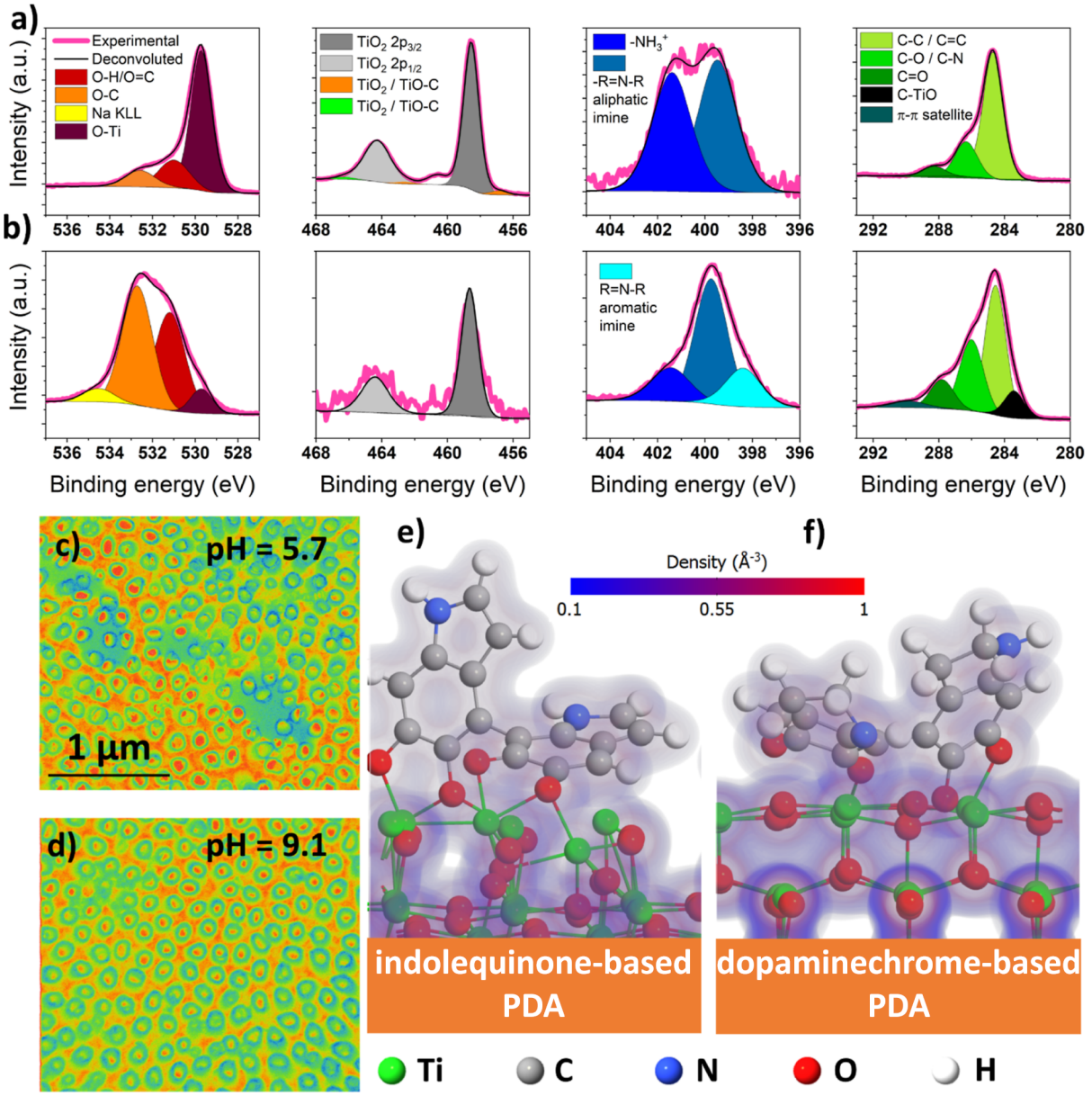

Figure 3. High-resolution XPS spectra of TNT|PDA with dopamine polymerized in (a) acidic pH (5.7) and (b) alkaline pH (9.1); SEM pictures of TNT|PDA with dopamine polymerized in (c) acidic pH (5.7) and (d) alkaline pH (9.1); DFT-optimized geometry of PDA adsorption on anatase TiO_2 slabs (101) along with electron density maps; PDA is modeled as a dimer of (e) IQ or (f) DC monomers.

is expected. At a slightly acidic pH, there is only one pair of redox peaks, with a gradually decreasing current density corresponding to the DA/DQ pair.[17,42,43] These signals lie at the potentials at 0.0 and +0.5 V, and the oxidative currents are higher, suggesting irreversibility of the oxidation. Under neutral conditions (7.5 pH), an additional signal at +0.25 V is manifested but only in the first cycle. In our previous work, we indicated that, during PDA electrodeposition, LDC/DC redox pair reactions are mainly observed in this potential range.[42] The shapes of the CV curves at this pH are in agreement with analogous experiments reported in the literature.[44,45] At a more alkaline pH between 9 and 10, there is only one complex oxidation peak between 0.0 and +0.8 V superimposed of several redox reactions, presumably of the LDC/DC and DHI/IQ pairs. Additionally, the current density decay is faster in alkaline pH and plummets to several μA cm^{-2} after 25 cycles. In an even more alkaline pH of 11 and above, the PDA coating is not formed, most probably due to delamination of the PDA layered structure in the presence of hydroxyl ions.[46,47]

Two different color contrasts of the SEM images were used to show changes in the morphology of the TNTs after electropolymerization (Figure 2a–d). In general, as-formed nanotubes have a wall thickness of 27.7 ± 5.9 nm. However, after modification, this value is on average 38.6 ± 6.9 nm. This indicates the formation of the layer on both the inner and outer walls of the nanotubes with an approximate thickness of 5.5 ± 1.0 nm. Visually, it is especially pronounced with the orange–green contrast of the SEM pictures. Tilted nanotubes are thickened not only at the corona but also along the shaft. It is a strong clue that PDA covers a large area of the nanotubes from the bottom to the top. Similar coverages were obtained with photo-electropolymerization of dopamine on TiO_2 nanorods.[48] Moreover, a set of SEM pictures of various areas of the sample at

https://doi.org/10.1021/acs.jpcc.2c08804
J. Phys. Chem. C 2023, 127, 12662−12677

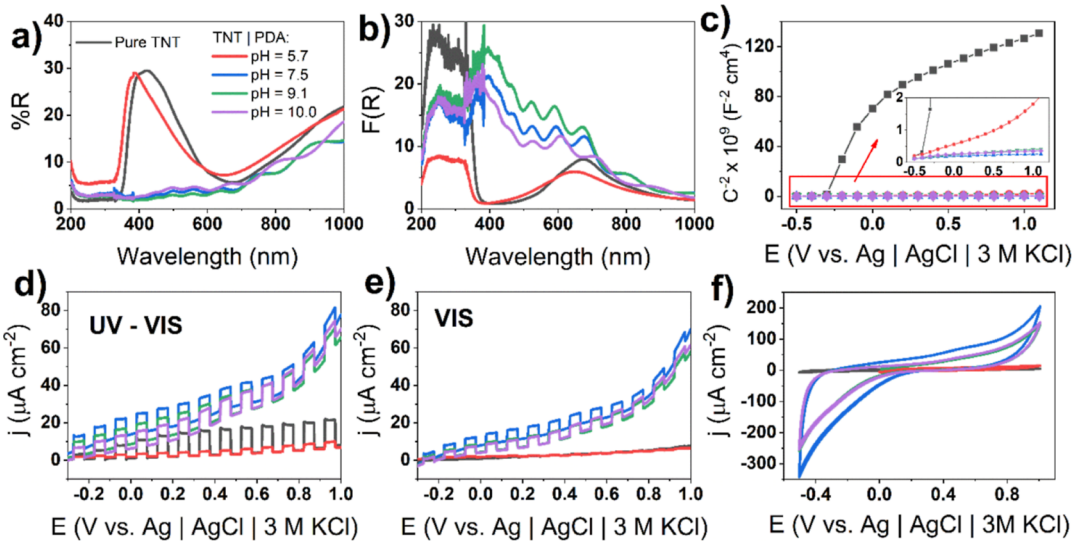

Figure 4. Comparison of optical and photoelectrochemical properties of 30 V TNT|PDA heterojunctions polymerized at different pH (50 CV cycles of polymerization); (a) reflectance spectra; (b) KM functions; (c) Mott−Schottky plot inset showing the range of low C^{-2} values; chopped dark−light LSV scans with a 20 mV/s scan rate, (d) illumination with a UV−vis light source, (e) vis light source, and (f) CV scans; the electrolyte for electrochemical experiments was 0.5 M Na_2SO_4.

different magnifications are presented to support this effect (Figures S1−S3).

3.2. XPS Studies of PDA Deposited on TNTs. Besides morphology, there are major differences in the chemical structure of TNT|PDA junctions depending on the pH used for electropolymerization (Figure 3a,b). First, in the oxygen part of the spectrum, three peaks are present for acidic PDA (TNT|a-PDA), which correspond to O−Ti (530 eV), C−O−H (531 eV), and O−C (533 eV) bonds, respectively. A significant increase in signals corresponding to C−O and O−H bonds—compared to the pristine nanotubes[27,49,50]—suggests the formation of PDA consisting mostly of catecholic units such as DA, LDC, and DHI. This is in agreement with the overall reaction scheme, where the presence of H^+ ions shifts the reaction toward catecholic products (eq 3)

$$R = O + H^+ + e^- \rightarrow R\text{-}OH \quad (3)$$

where R stands for the ring of the PDA units. However, the basic PDA (TNT|b-PDA) exhibits an additional peak at 535 eV corresponding to C═O bonds. This suggests the presence of a strong contribution of quinone-containing units such as DQ, DC, and IQ in the structure.

The titanium region shows six peaks for TNT|a-PDA and only two for TNT|b-PDA. All signals are characteristic of pristine TNTs[27,49,50] but are notably smaller for TNT|b-PDA. This is justified by the higher coverage of the nanotubes in b-PDA, which leads to quenching of the XPS signal. The quantitative data of the atomic surface composition is given in Table S1. It is easy to see that the total contribution of Ti in acidic PDA is 16.41%, while it equals only 0.33% in case of basic PDA. On the other hand, the total carbon content for b-PDA is twice as high and the nitrogen content is tripled. Considering that the XPS signal originates from approx. 1−5 nm beneath the surface, the anticipated cause of the weaker Ti 2p signal in an alkaline environment is the larger thickness of the PDA coating and higher degree of uniformity. In terms of morphology, a-PDA is found in the form of islands and several nanotubes remain bare, while b-PDA uniformly covers the walls of most of the nanotubes.

Detailed studies and discussions on the uniformity of PDA on different length scales can be found in the Supporting Information. SEM images with numerous magnifications and contrasts recorded on different areas of the TNT_bPDA sample are displayed in Figures S1−S3, revealing uniformly distributed PDA across the surface. Furthermore, Raman maps of the ratio of the G, D, and A bands at micrometer and millimeter scales (Figures S4−S7) were studied. The G-to-A band map showed that over 80% of the sample areas exhibit a ratio of 3.4 to 4.5, while the G-to-D map exhibited a 1.4 ratio across 98% of the surface, both implying the phase uniformity of PDA. Several islands deviating from the average ratios indicate that the uniformity is not perfect, although it can be considered satisfactory for the proposed photoelectrochemical investigations. Next, uniformity analyses were supported by spatially and spectrally resolved photocurrent maps (Figure S8) and macroscopic images of the TNT_bPDA samples (Figure S9). Therefore, uniformly coated PDA hinders the signal from the TiO_2 substrate and leads to the increased signal of carbon and nitrogen. Quantitative results for oxygen are inconclusive in this context because both PDA and TiO_2 contain oxygen atoms in different electronic environments.

Examination of the nitrogen region of the XPS spectra reveals two peaks for TNT|a-PDA located at 399 and 401 eV, attributed to R═N−R aliphatic imine and R−NH_3^+ groups, respectively. Alternatively, the 399 eV signal could originate from R−NH−R aliphatic groups of LDC and DC units, which are suspected to be dominant in TNT|a-PDA.[11,42] An additional peak at 398 eV, observed only for TNT|b-PDA, was attributed to the R═N−R aromatic imine or aromatic R−NH−R amine, both of which are known to be present in the structure of alkaline-based PDA.[3] This is strong evidence that a-PDA contains more aliphatic amines/imines than b-PDA, indicating the higher content of DHI and IQ conjugated units in b-PDA, which was reflected in computational models.

Lastly, three peaks are found in the carbon region for TNT|a-PDA, attributed to C−C and C═C bonds, collectively, at 284 eV, C−O and C−N bonds at 286 eV, as well as C═O bonds at 289 eV. On the other hand, TNT|b-PDA exhibits two additional

https://doi.org/10.1021/acs.jpcc.2c08804
J. Phys. Chem. C 2023, 127, 12662−12677

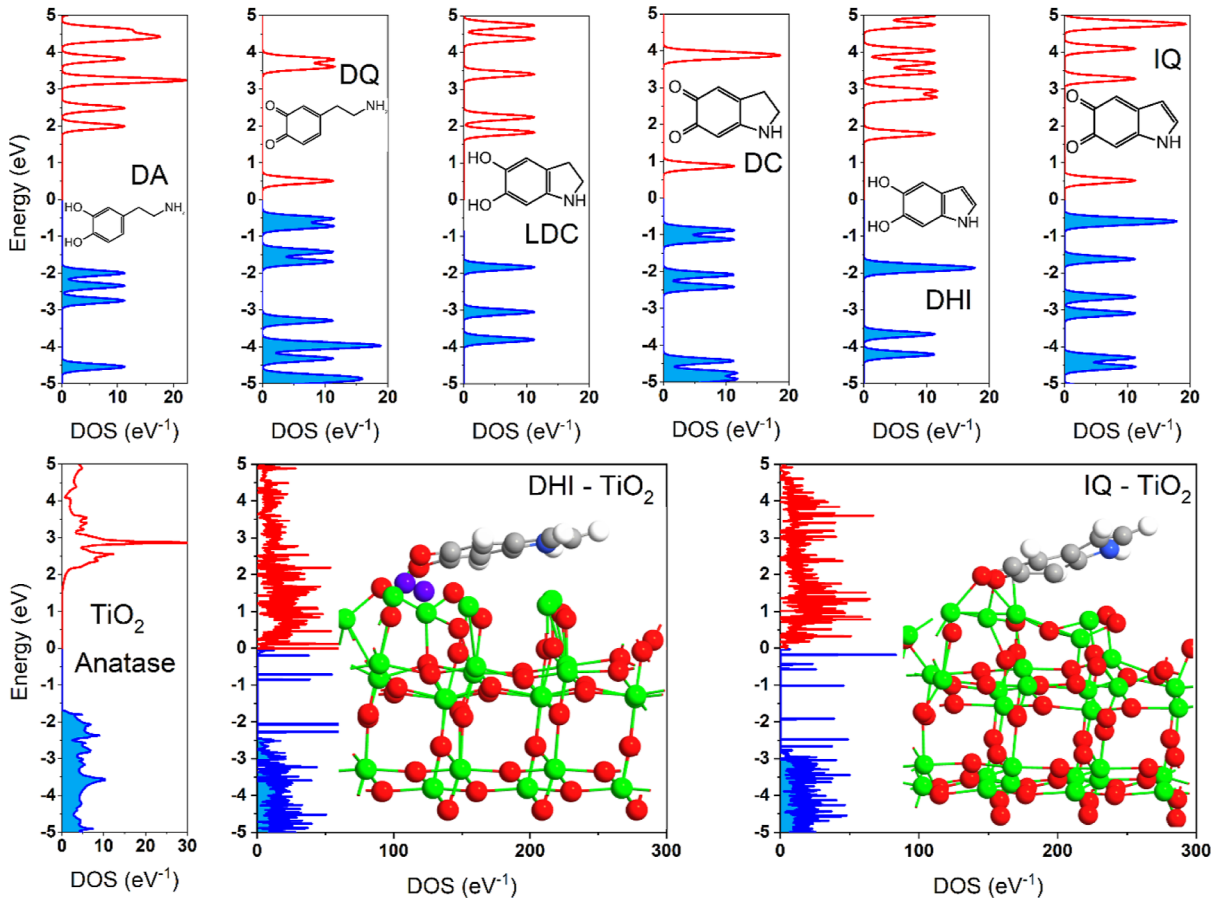

Figure 5. DOS spectra for six different structural units of PDA: dopamine (DA), DQ, LDC, DC, DHI, and IQ; for pristine bulk anatase; for anatase with adsorbed DHI and anatase with adsorbed IQ. The Fermi energy is at zero; filled states are marked in blue and empty in red. The surface used for adsorption is anatase (101), and the atom colors are the same as in Figure 3.

peaks at 283 and 291 eV, attributed to C−TiO bonds and $\pi-\pi$ shakeup satellite peaks, respectively. A higher share of the C═O peak for TNT|b-PDA suggests a higher content of quinone forms and the presence of $\pi-\pi$ shakeup satellite peaks, which provides additional evidence of the strong contribution of π-conjugated DHI and IQ units in b-PDA but not in a-PDA.

The unique nature of C−TiO bonds can be justified by DFT calculations of the PDA adsorption on the surface of TiO_2 (Figure 3e,f). In this simulation, two types of PDA dimers (indolequinone IQ−IQ and DC−DC dopaminechrome) were relaxed on the surface of anatase (101). IQ−IQ can be considered as a model for b-PDA and DC−DC for a-PDA because the registered electropolymerization CV curves and data from the literature indicate that these units are expected to dominate in PDA obtained in alkaline solutions.[11,42] After optimization, several Ti−O−C surface bonds can be found for both types of PDA, and the high overlap of the electron densities strongly suggests their relatively strong character. In general, PDA subunits attain an equilibrium position so that the surface Ti atom lies below the ring. There is a strong overlap in electron densities between adjacent Ti and C atoms with lengths of 2.41−2.64 A for IQ−IQ and 2.35−2.38 A for DC−DC structures, suggesting nontrivial surface Ti−C bonding. These lengths are smaller than for typical $\pi-\pi$ interactions (on the order of 3 Ang and higher) but larger than in the case of typical C−C covalent bonds (1.8 Ang and lower). Therefore, the binding energy of the abovementioned Ti−C bond is anticipated to be smaller than C−C. As a result, such a molecular arrangement of PDA subunits might explain the atypical peak at the carbon part of the XPS spectrum at 283 eV. Moreover, such a bond might be the origin of interactions described as Ti−O−C in Ti 2p spectra. These observations suggest that the DC−DC type of PDA has a slightly stronger affinity toward the surface of anatase, but Ti−C bonds are present in both types.

In general, XPS studies indicate that PDA electropolymerized under slightly alkaline conditions exhibits a higher content of quinones and conjugated units such as IQ involving R═N−R imines and R−NH−R amines compared to PDA synthesized in a slightly acidic environment.

3.3. Influence of Electropolymerization pH and Nanotube Geometry on Optical and Photoelectrochemical Properties of TNT|PDA Heterojunctions. The pH of the electropolymerization solution plays a tremendous role in tailoring the adsorption and chemistry of PDA. Figure 4 indicates that it also has a significant effect on the optical and photoelectrochemical properties of the TNT|PDA junctions. UV−vis reflectance spectroscopy data, as well as KM function plots (Figure 4a,b), clearly show that pristine nanotubes exhibit a pronounced absorption edge that starts at ca. 380 nm in the UV region followed by a broad band in the visible and near-infrared (NIR) range (500−900 nm). Subsequent spectra of TNT|PDA polymerized at pH = 5.7 resemble pristine PDA to a large extent, with a notable reduction in the absorption intensity at the band edge (Figure 4b). However, when the pH of electropolymerization was neutral or slightly alkaline, the

https://doi.org/10.1021/acs.jpcc.2c08804
J. Phys. Chem. C 2023, 127, 12662−12677

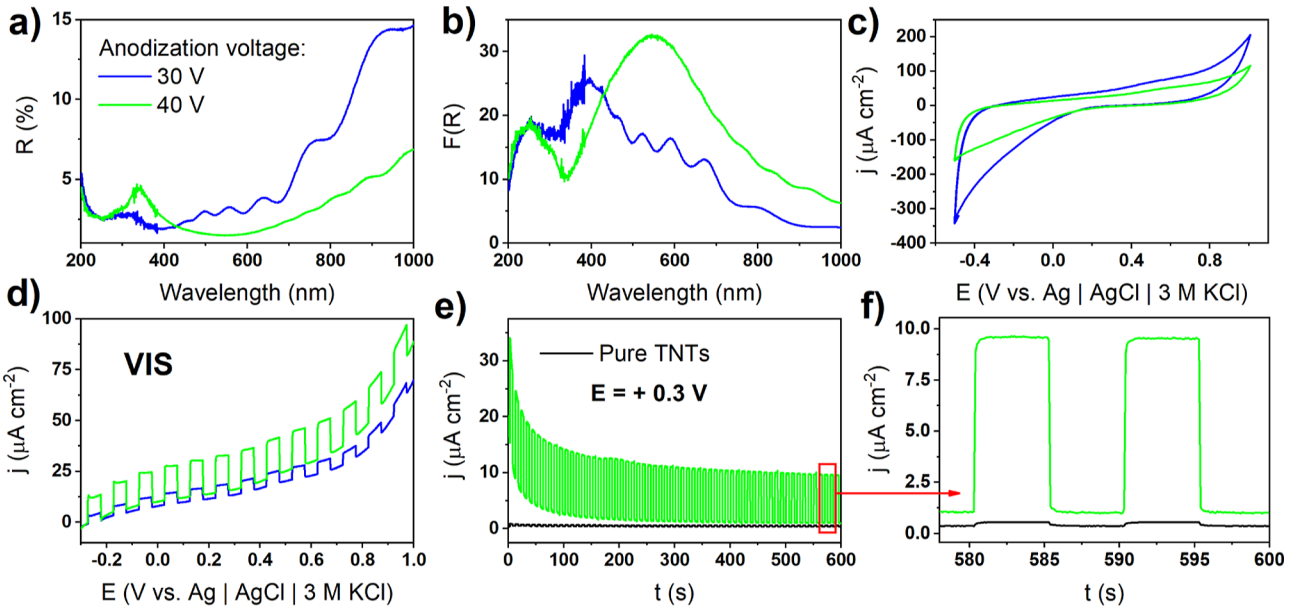

Figure 6. Comparison of the optical and photoelectrochemical properties of TNT|PDA heterojunctions with different nanotube dimensions resulting from various anodization voltages. Polymerization of dopamine was performed in pH = 8.5 and with 50 CV cycles; (a) reflectance spectra; (b) KM functions; (c) CV scans; (d) chopped dark−light LSV scans with 20 mV scan and visible-range light source; (e) chopped dark−light CA curves; (f) inset at a steady state; 0.5 M Na_2SO_4 was used as an electrolyte.

emergence of several peaks is observed in the visible and NIR range, with a simultaneous decrease of the absorption edge. The origin of these peaks is either from the presence of discrete energy levels introduced into the system through electropolymerization[15] or the geometry-dependent scattering observed in several works.[51,52] Moreover, the enhancement of the spectral signal in the visible range is larger compared to the other works reporting modification of TiO_2 with PDA.[48,53]

The described effects also have a profound influence on the photoelectrochemical activity (Figure 4d,e). LSV curves recorded under cyclic dark−light exposure during polarization show that there is an increase in photocurrents after modification of pure nanotubes in the potential range from −0.2 to +1.0 V. This improvement is observed only when PDA is polymerized at a pH of 7.5 or greater. Interestingly, the magnitude of the photocurrents is almost equal in either UV−vis or solely vis conditions. In other words, pristine nanotubes have poor photoactivity in visible light and decent photoactivity in UV−vis, while TNT|PDA structures have roughly the same photoactivity regardless of the UV component. These observations agree well with the presence of peaks in the KM functions in the visible range. This is therefore another strong clue that absorption bands in the visible range stem from discrete energy levels of PDA and, in turn, cause enhancement of photocurrents.

Additionally, the application of a PDA layer causes an increase in the background (dark) currents. A comparison of CV curves registered under dark conditions (Figure 4f) shows that these currents are mostly capacitive, which has been reported in the literature.[54] Additionally, the Faradaic currents of the quinone-catechol redox reactions are also notable at +0.5 and −0.2 V.[42] To compare the electrical properties of pure nanotubes with those modified with PDA, Mott−Schottky plots (Figure 4c) were constructed. Surprisingly, after electropolymerization, there is no change in the inverse squared capacitance C^{-2} with the electrode potential, which is a characteristic effect for a semiconductor.[55] Therefore, the flat-band potential does not exist for TNT|PDA structures. The hypothesis is that the application of PDA on TiO_2 nanotubes shifts the surface electrical properties from an n-type semiconductor to a semimetal. Interestingly, although PDA deposited at pH 5.7 does not cause significant changes in the optical properties and photocurrents, it still shifts the electrical character of the TNT|PDA heterojunction (Figure 4c, red curve).

The relations observed in the UV−vis spectra and electrochemistry can be better understood through the analysis of the DOS plots of different PDA structural units (Figure 5). First, the HOMO−LUMO gap is equal to 3.4−3.8 eV for catecholic units (DA, LDC, and DHI) and there are only slight differences between them.[56] Considering that the XPS spectra coupled with the electrochemistry and DFT adsorption simulations showed that a-PDA consists mainly of catecholic units, its high HOMO−LUMO gap is responsible for the negligible effects on the UV−vis characteristics (Figure 4a−c) and reduced photoactivity. However, quinone structural units (DQ, DC, and IQ) exhibit significantly smaller gaps, ranging from 0.7 to 1.4 eV, which consequently lead to enhancement of the absorption and photoactivity. A similar effect was also observed in the work of Zou et al.[15]

Moreover, when PDA structural units are adsorbed on the surface of anatase (101), the density of surface states changes remarkably. The DOS of pristine anatase exhibits well-separated conduction and VBs with a ca. 3.5 eV gap. However, when the PDA unit is adsorbed on its surface, several states are formed between the bands and the type of adsorbent strongly determines their number, position on the energy scale, and electronic population. In particular, the IQ-TiO_2 junction exhibits a larger contribution of intraband states. Additionally, more states in the conduction band and near its edge are populated with electrons, which is another argument for a semimetallic character of the TNT|PDA junction and for the observed photosensitization effects.[47]

A crucial factor influencing the optical and photoelectrochemical properties of TNT|PDA structures is the geometry of

https://doi.org/10.1021/acs.jpcc.2c08804
J. Phys. Chem. C 2023, 127, 12662−12677

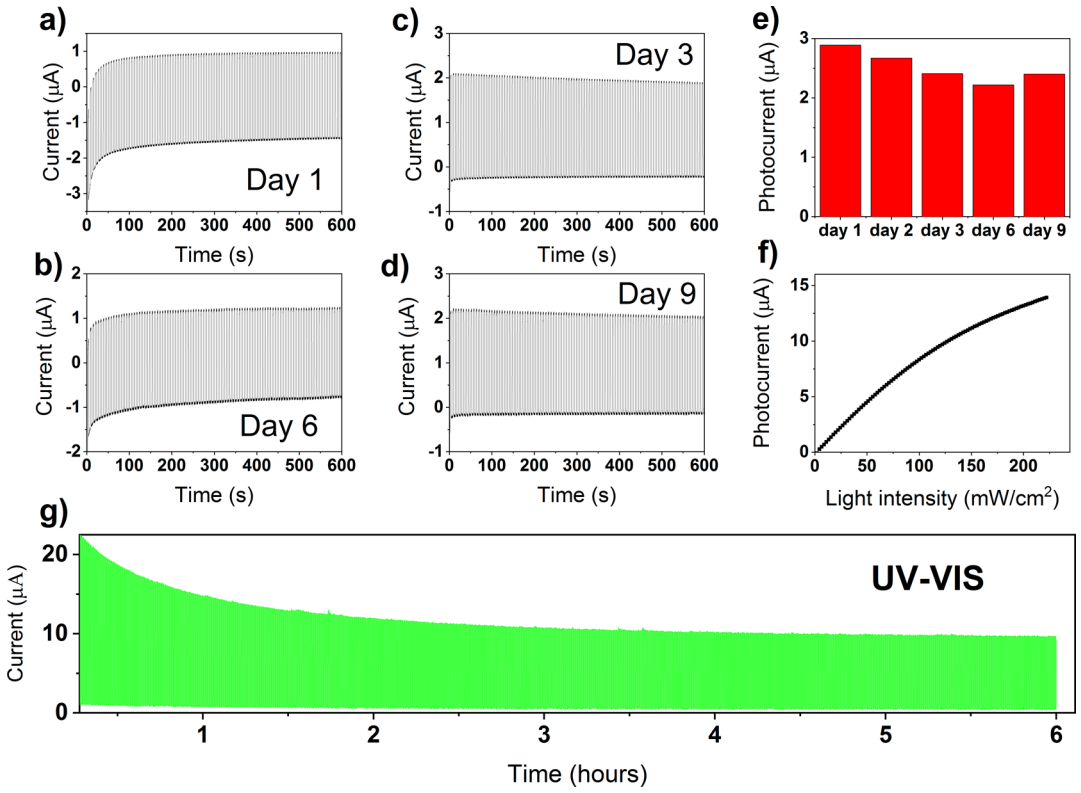

Figure 7. (a–d) Transient photocurrents of the TNT_bPDA sample registered during 9 days; (e) photocurrent change during the course of measurements; (f) intensity profile of the photocurrent—100% intensity equals to 2.2 mA cm^{-2} power density; (g) transient photocurrents measured continuously during the 6 h exposure to the mixed UV–vis light. All measurements were performed in a three-electrode configuration with 0 V vs Ag|AgCl polarization.

the nanotubes. Manipulation of the anodization voltage is a versatile tool to adjust the nanotube dimensions. In particular, 30 V TNTs have a 700 nm length and a 110 nm diameter, while 40 V TNTs have a 1100 nm length and 160 nm diameter on average.[27] Considering the promising photosensitization capabilities of PDA, the geometry of the nanotubes was optimized to obtain the highest photocurrents in the visible range. The reflectance spectra of TNT|PDA with different TNT geometries, but the same route of PDA deposition, are given in Figure 6a (30 V are represented as blue and 40 V as green curves). For this comparison, the electropolymerization pH was optimized to 8.5 and the number of polymerization cycles was 50. The optical spectra and KM functions show clearly that 40 V TNT|PDA junctions—with wider and longer nanotubes—have higher absorption in the visible range. Additionally, instead of several small absorption bands, there is a single, wide band centered at ca. 550 nm, presumably originating both from changes in the electronic structure and the geometry-dependent scattering.[51,52] The issue of deconvolution of these two effects will be discussed further on the basis of IPCE spectra.

The LSV curves registered during the dark–light cycling (Figure 6d) indicate that 40 V TNT|PDA exhibit photocurrents 3 times higher than 30 V TNT|PDA in the visible range. This fact correlates with the higher absorption edge (lower reflectance). Prolonged potentiostatic polarization at a potential of +0.3 V (Figure 6e) shows that the TNT|PDA exhibits decay of dark current according to the Cotrell equation (i.e., inversely proportional to time), but after ca. 8 min, a steady state is achieved. The PDA modification increases photocurrents by ca. 20 times compared to pristine TNTs. In the steady state (Figure 6f), a magnification from 0.5 to 10 μA cm^{-2} is observed. This effect, attributed to the absorption by discrete levels of PDA, is greater than previously observed in the literature for TiO_2|PDA junctions.[48] Presumably, the key factor explaining the difference is hydrogenation before PDA deposition. Although this information is insufficient to conclude that PDA is stable after UV light exposure, another set of studies have been performed to verify this issue and have been exhaustively discussed in the Supporting Information. In brief, XPS and SEM pictures recorded after 100 cycles of UV exposure strongly suggest that no major changes in morphology and surface chemistry can be detected (Figures S10 and S11). Moreover, TNT_bPDA retains its optical properties and capability of photocurrent generation at a constant level even after 9 days of measurements and 6 h of continuous polarization and UV–vis exposure (Figures S12, S13, and 7).

Another difference between the electrochemical properties of TNT|PDA depending on the nanotube geometry was noticed. The CV results in Figure 6c show that the capacitive currents of 30 V TNT|PDA are noticeably higher than those of 40 V TNT|PDA. However, in the LSV curves in Figure 6d, the relationship is the opposite and the dark capacitive currents of 30 V TNT|PDA are smaller. Moreover, the dark capacitive currents of 40 V TNT|PDA increase faster with applied potential than those of 30 V TNT|PDA. This behavior suggests that there could be some photoinduced charging of 40 V TNT|PDA leading to the increase of capacitive currents.[57] Presumably, during light exposure, ionic excited states (e.g., anionic radicals) are created in the PDA layer, and thus, the surface charge is generated, which does not decay in the second timescale of the experiment.

The stability of photocurrents was assessed using various methods. Initially, the transient photocurrents of a single sample

https://doi.org/10.1021/acs.jpcc.2c08804
J. Phys. Chem. C 2023, 127, 12662–12677

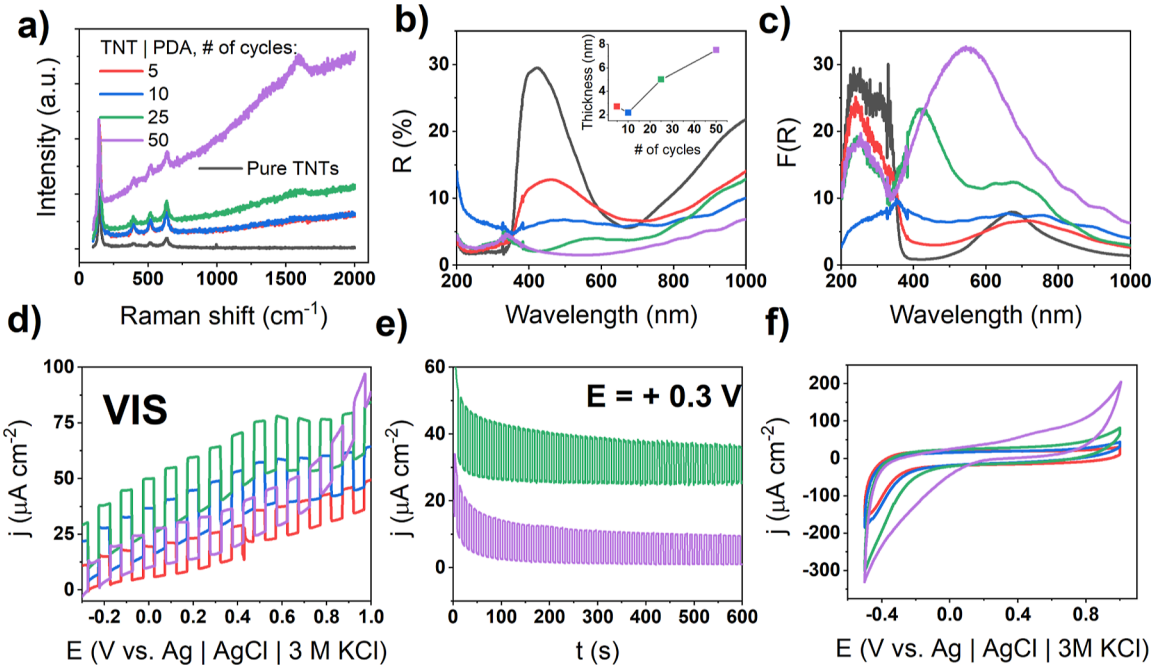

Figure 8. Comparison of optical and photoelectrochemical properties of 40 V TNT|PDA heterojunctions with different thicknesses of PDA; (a) Raman spectra and (b) reflectance spectra (inset shows the relationship between the number of polymerization cycles and thickness of PDA measured by SEM); (c) KM functions; (d) chopped dark−light LSV scans with a 20 mV scan and visible-range light source; (e) chopped dark−light CA curves for 25 times cycled and 50 times cycled TNT|PDA; (f) CV scans; 0.5 M Na_2SO_4 was used as an electrolyte.

were measured over a span of 9 days while exposing it to UV light from an LED with an intensity of 2.2 mW/cm^2. Each day was analyzed separately, as depicted in Figure 7a−f. It is evident from the results that the TNT_bPDA sample maintains a relatively stable photocurrent response. This suggests that the sample does not experience significant degradation when stored or repeatedly exposed to UV light, electrolytes, or oxygen. Additionally, the response of the TNT_bPDA sample to a combination of UV−vis light was examined during a 6 h transient measurement, as shown in Figure 7g. Over time, a Cottrellian decay of the total current is observed, affecting the photocurrents in the initial 2 h. However, after this initial period, the response stabilizes and remains mostly unchanged for the following 4 h.

3.4. Influence of PDA Thickness on Optical and Photoelectrochemical Properties of TNT|PDA Heterojunctions. The thickness of PDA depends on many factors such as the solvent, ionic environment, and synthetic approach,[11,12,58,59] which have a profound role in the properties of the semiconductor|PDA heterojunctions.[23,25] In our work, the thickness of the PDA electropolymerized in TiO_2 is almost linearly dependent on the number of CV cycles during electropolymerization with the limiting value of ca. 8 nm (inset in Figure 8b). Similar behavior was observed in the work of Kund et al.[59] Diffuse reflectance spectra and KM functions show that as the PDA thickens, absorption in the visible range is more pronounced and the band-to-band absorption edge plummets (Figure 8b,c).

Raman spectra show several characteristic bands of anatase for both pristine TNT and all TNT|PDA samples.[27,50] However, with the increasing PDA thickness, additional D and G bands of sp^2 rings emerge and the relative intensity with respect to anatase signals drastically increases (Figure 8a). The observed D and G bands are especially pronounced for the thickest PDA layer, with a significant increase of the baseline, indicating fluorescence[60] (see the Raman maps shown in Figures S4−S7).

The magnitude of photocurrents in the visible range is the smallest for 5-cycled PDA (13 μA cm^{-2}), which then increases (to 30 μA cm^{-2}) for 25-cycled TNT|PDA and slightly decreases for 50-cycled TNT|PDA (25 μA cm^{-2}). On the one hand, the photocurrent baseline is twice as high for 25-cycled TNT|PDA with respect to 50-cycled TNT|PDA, and on the other hand, dark CV currents show that the capacitive currents are higher for the thickest PDA (Figure 8d−f). This increase again suggests a photocharging effect in the PDA layer with a 5 nm thickness with nonvanishing charges in the timescale of the experiment.[57]

Enhancement of the photocurrent response by PDA was further confirmed by quantum efficiency measurements (Figure 9a−c). The IPCE map registered for pristine TNTs exhibits a characteristic band edge starting at 400 nm with a maximum at 350 nm (80% efficiency) for a wide range of polarizations (0−1200 mV vs Ag|AgCl|3 M KCl). Zero efficiency is observed for wavelengths longer than 410 nm. The magnitude of the IPCE maximum remains almost constant regardless of the applied potential. However, when TNT|PDA structures are considered, an additional small IPCE band emerges in the whole visible spectrum, with a maximum at 450 nm reaching 9% IPCE for the 25-cycled sample and 14% for the 50-cycled sample. The presence of this peak explains the photocurrent enhancement after the application of the PDA coating. These enhancements in the visible region can be observed in detail on the transient photocurrent plots recorded for different wavelengths and several samples, strongly suggesting that the phenomenon is universal to the proposed PDA modification. Furthermore, the IPCE maximum for the TiO_2 band edge is smaller for TNT|PDA and increases with the applied anodic potential. Presumably, because PDA covers the nanotube walls, most of the photon absorption occurs inside the PDA layer, so band-to-band transitions are quenched. Additionally, oxidization of PDA leads

https://doi.org/10.1021/acs.jpcc.2c08804
J. Phys. Chem. C 2023, 127, 12662−12677

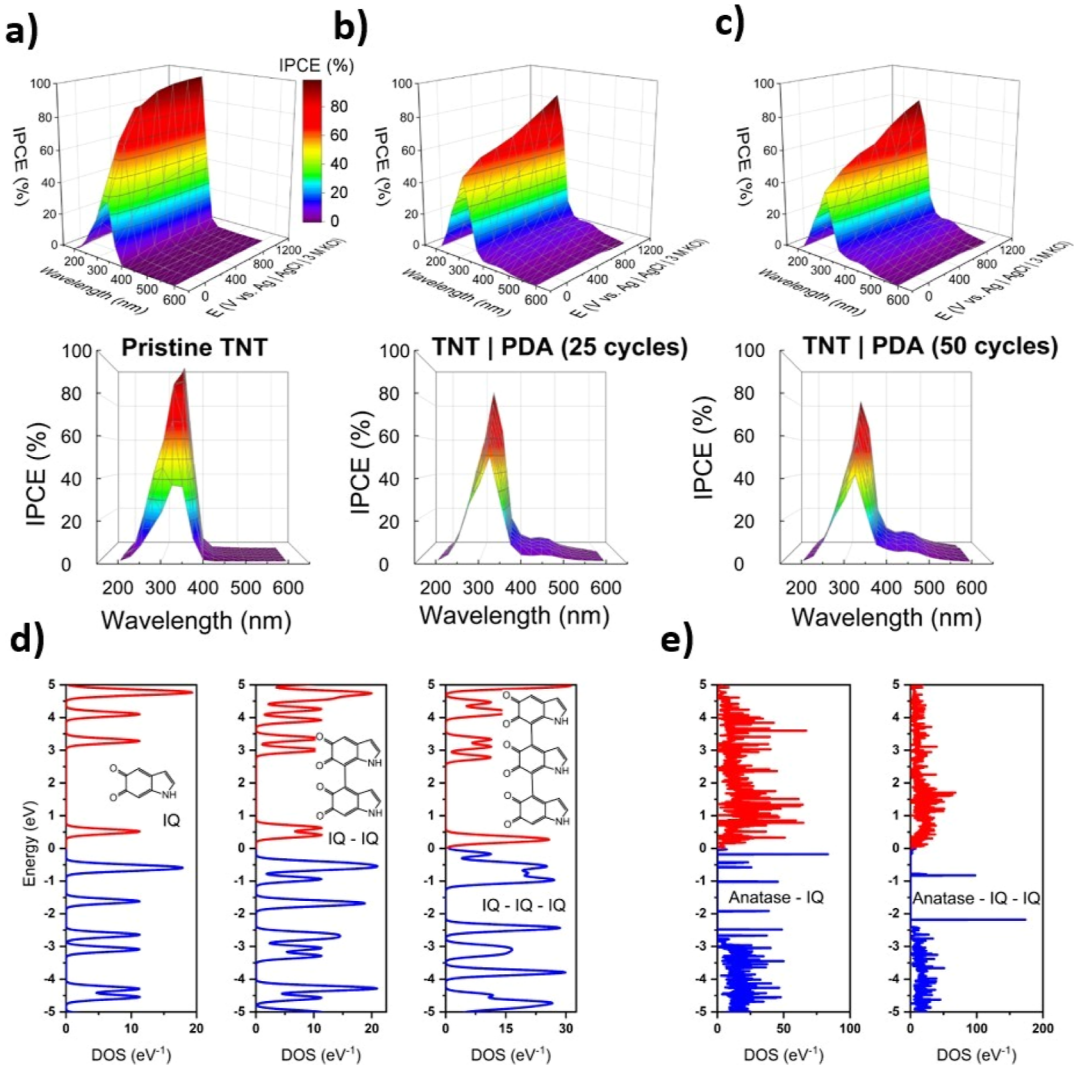

Figure 9. Comparison of quantum efficiency maps of 40 V TNT|PDA heterojunctions with different thicknesses of PDA, (a) pure TNTs, (b) 25-cycled TNT|PDA, (c) 50-cycled TNT|PDA, (d) DOS spectra of the isolated PDA monomer (IQ), dimer (IQ–IQ), and trimer (IQ–IQ–IQ); (e) DOS spectra of the PDA monomer and dimer adsorbed on the anatase (101) surface.

to the increased contribution of quinone units, which have a lower HOMO–LUMO gap (Figure 5), so the absorption rate is higher, and therefore, the IPCE is higher. The thickest PDA layer (TNT|PDA 50 cycles) results in a higher magnitude of the IPCE in the visible part of the spectrum, which correlates well with the changes observed in the reflectance spectra (Figure 8b,c).

DFT-based DOS spectra of PDA with variable chain lengths were computed for further elucidation of its thickness-dependent photoelectrochemical properties (Figure 9d). It is easy to see that the HOMO–LUMO gap decreases from 0.7 eV for one unit of PDA to basically 0.0 eV for three units of PDA. This is because the density contributions from π orbitals of the conjugated system overlap. This behavior would explain the experimentally observed fact that a larger amount of polymerization cycles during PDA synthesis leads to greater enhancement of optical absorption (Figure 8b,c). As shown in Figure 5, when PDA units are adsorbed on the anatase surface, several intraband energy levels emerge and the edges of the conduction and VBs are smeared out. Interestingly, single-unit PDA introduces up to 8 intraband states, while double-unit PDA introduces only two states, but their electronic population is markedly higher (Figure 9e). Moreover, the energy distance between the most highly populated intraband state and the conduction band of the anatase equals 2.2 eV, which corresponds to a 550 nm wavelength—almost exactly at the onset of the IPCE band for TNT|PDA structures. Therefore, IPCE analysis in conjunction with DFT calculations gives strong evidence that intraband states introduced by the PDA increase the photoactivity of TNT|PDA in the visible range.

3.5. Semimetallic Character of the TNT|PDA Interface.

So far, several sets of data, including reflectance spectra, Mott–Schottky plots, DFT analysis, and quantum efficiency maps, have suggested that the TNT acquires a semimetallic character after modification with PDA. This section focuses on an in-depth analysis of the properties of this interface by employing the electrochemistry of ferrocyanides in a standard and nonlinear approach. Figure 10a shows the first 10 cyclic voltammograms of TNT|PDA when exposed to a 5 mM solution of ferrocyanides. The first cycle consists of two symmetric redox peaks located at +0.15 and +0.35 V. Although the peak separation is 200 mV, and therefore the reaction is irreversible, this curve resembles the response characteristic of metallic surfaces, such as gold and platinum.[61] However, with

https://doi.org/10.1021/acs.jpcc.2c08804
J. Phys. Chem. C 2023, 127, 12662–12677

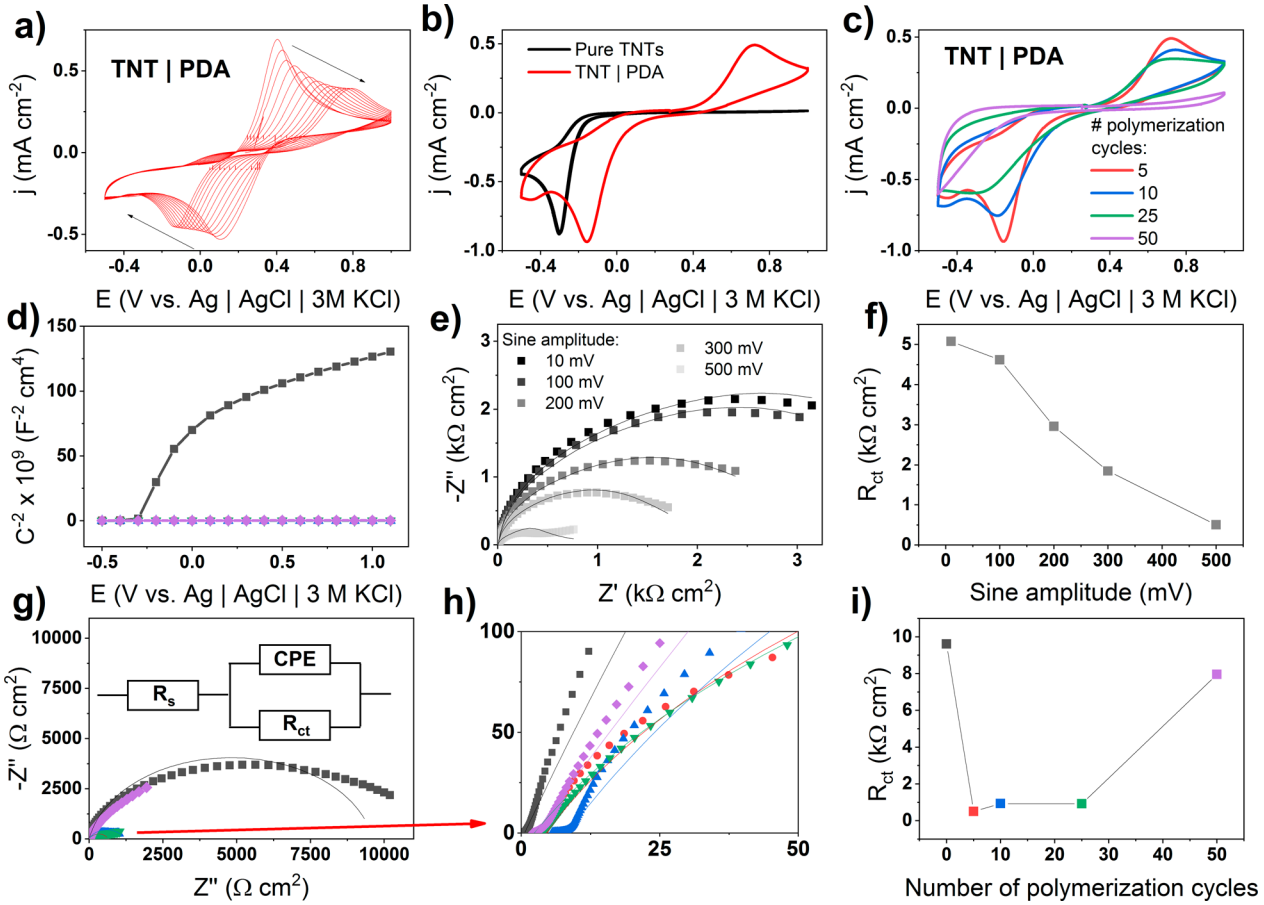

Figure 10. Investigations of the electrical and electrochemical properties of the TNT|PDA heterojunction; (a) 10 subsequent CV cycles (50 mV/s rate) of TNT|PDA in 5 mM ferrocyanides; (b) comparison of ferrocyanide response of TNTs and TNT|PDA after stabilization; comparison of (c) ferrocyanide response and (d) Mott−Schottky plots for TNT|PDA with different thicknesses of PDA; (e) NL-EIS spectra of TNT|PDA recorded in 5 mM ferrocyanides with different amplitudes of stimulating single-sine voltage; (f) nonlinear relationship between charge-transfer resistance and amplitude of stimulating voltage; (g−i) comparison of EIS spectra for TNT|PDA with different thicknesses of PDA and the relationship between charge-transfer resistance and thickness of PDA [supporting electrolyte was always 0.5 M Na_2SO_4; the equivalent circuit for all fitting was the one depicted in (g)].

consecutive cycling, the peak separation increases, and the symmetry is lost—the reduction peaks are slightly larger. After ca. 10 cycles, the CV curves are stabilized with a peak separation equal to ca. 850 mV.

The ferrocyanide response of pure TNT consists only of the reduction peak at −0.33 V (Figure 10b) as TiO_2 is an n-type semiconductor with a wide band gap and an oxidation peak is expected. However, after PDA modification, this peak is shifted toward more positive potentials and an oxidation peak is also present. These data further strongly suggest that the PDA introduced a set of energy levels associated with surface midgap states, effectively changing the character of the titania surface toward semimetallic while preserving the capability of photocurrent generation through the separation of charge carriers in the space charge region of TiO_2. The hypothesis is that the quinone/catechol redox pairs abundant in the PDA chain play a crucial role as redox mediators that enable charge transfers in the energy range inside the band gap.[16,62,63] In other words, even in dark conditions, holes of the VB migrate to the surface states of the TNT and oxidize catechols to quinones. These quinones are then capable of oxidizing ferrocyanides, which was energetically impossible for direct oxidation by VB holes. Consecutive cycling increases the potential difference between the ferrocyanide peaks (Figure 10a) presumably due to depletion of surface states—fewer surface states occupied by holes lead to less oxidation of catechols and a higher energetic barrier for the oxidation of Fe(II) to Fe(III).

Figure 10c shows differences in the response for various thicknesses of PDA. 5-Cycled, 10-cycled, and 25-cycled samples have similar responses with a notable decrease in the magnitude of the redox peaks with the PDA thickness. However, for a 50-cycle sample, the redox response is completely diminished. The hypothesis explaining this phenomenon is that when the PDA thickness reaches a certain threshold (in this case, 8 nm), electron transfer processes are quenched; i.e., electrons can no longer tunnel through the PDA layer. This behavior was observed frequently in other works, but the limiting thickness is dependent on the substrate semiconductor material.[23,25,54] In other words, regardless of the hole oxidizing the catechol on the TNT side of the PDA, the electron from the Fe(II) cannot tunnel through the other side of the PDA to complete the reaction. Therefore, the Fe(II) stays reduced and there are no oxidation current peaks on the CV curves. Interestingly, the Mott−Schottky analysis shows that all TNT|PDA interfaces exhibit a semimetallic character regardless of the thickness of PDA (Figure 10d). Supposedly, while the ferrocyanide response involves charge transfer and tunneling of the electrons, the Mott−Schottky analysis utilizes information mostly about the

https://doi.org/10.1021/acs.jpcc.2c08804
J. Phys. Chem. C 2023, 127, 12662−12677

double-layer structure. Therefore, there is no upper limit in the tunneling distance, and the double-layer structure of TNT|PDA remains semimetallic regardless of the thickness.

For further investigation of the TNT|PDA electrical properties, EIS was employed in the nonlinear potential regime (NL-EIS). In this setup, very high amplitudes of the potential stimulus were applied purposely, so the higher-order effects would occur.[64] The equivalent circuit for fitting was the Randles circuit with a constant-phase element (CPE), i.e., R(CPE,R), in Figure 10g. The fitting procedure was conducted using open-source EIS spectrum analyzer software.[65]

Figure 10e shows the NL-EIS first harmonic spectra registered in 5 mM ferrocyanides for a 10-cycled electrode (2 nm-thick PDA) with different sine amplitudes of 10 to 500 mV. Before each NL-EIS measurement, the TNT|PDA specimen was polarized for 3 min at the formal potential of the ferrocyanide redox pair. It is easy to see that the sizes of the semicircles are gradually decreasing with the amplitude. The explanation is that higher amplitudes allow the potential to sweep to the vicinity of the oxidation and reduction peaks (see Figure 10b). As a result, with higher amplitudes, more Faradaic current is registered, and thus, the polarization resistance is lowered. Inevitably, charge-transfer resistance also decreases with amplitude, almost linearly in the wide range of potentials (Figure 10f and Table S1). According to the Butler–Volmer theory, a Faradaic current for a single reaction during strong oxidative polarization is given by eq 4[61]

$$I = FADk^0 \exp\left(\frac{(1-\alpha)n\mathrm{F}}{RT}\eta\right) = I^0 \exp(A\eta) \tag{4}$$

where F is the Faraday constant, A is the electrode surface, D is the diffusion coefficient of ferrocyanides, k^0 is the kinetic constant, α is the Butler–Volmer charge transfer coefficient, R is the universal gas constant, and η is the overpotential. In this theory, the differential charge-transfer resistance is given by eq 5[61]

$$R_{\mathrm{ct}} = \frac{\mathrm{d}\eta}{\mathrm{d}I} = \frac{\exp(-A\eta)}{I^0 A} = \frac{1}{I^0 A}\left(1 - A\eta + \frac{(A\eta)^2}{2} - \frac{(A\eta)^3}{6} + \ldots\right) \tag{5}$$

Considering that the experimental potential amplitude was up to 0.5 V, which is a strong oxidation polarization, this equation is valid. The linear term is negative, which represents a decrease in the charge-transfer resistance with applied positive potential, which is observed in the experiment. However, the expected dependence of the charge-transfer resistance is exponential and not linear. Therefore, two sources of nonlinearity must be present in the experimental system, so the higher-order terms in the Taylor expansion can cancel out, leaving a linear dependence. The first of them is the oxidation of ferrocyanides. Based on the chemistry of PDA, the second source is hypothesized to be catechol/quinone reactions that are localized across the PDA chain.[15,66] The following simplified mechanism of the ferrocyanide electrochemistry on the TNT|PDA surface is proposed in eqs 6 and 7

$$\mathrm{Fe(CN)_6^{4-}} + \mathrm{R{=}O} + \mathrm{H^+} \rightarrow \mathrm{Fe(CN)_6^{3-}} + \mathrm{R\text{-}OH} \tag{6}$$

$$\mathrm{R\text{-}OH} + \mathrm{h^+} \rightarrow \mathrm{R{=}O} + \mathrm{H^+} \tag{7}$$

First, there is a proton-coupled chemical step, and the electron is transferred from ferrocyanide to quinone. As a result, quinone-PDA is transformed into catechol-PDA. Then, there is an electrochemical step that involves hole transfer from the VB to the catechol-PDA, effectively regenerating quinone-PDA. The anodic current registered during the voltammetry of TNT|PDA presumably comes from the reduction of quinones by Fe(II) being oxidized, and the cathodic current comes from the oxidation of catechols by Fe(III) being reduced.

With regard to the experimentally and theoretically discussed properties, we propose an alternative view of the electrochemistry of PDA|semiconductor interfaces. In this model, the PDA structural units behave as a set of spatially distributed redox mediators or as an electroactive polymer, rather than as a semiconductive polymer. This viewpoint explains why a slight change in the thickness of PDA leads to huge differences in the electrical and electrochemical properties of the TNT|PDA junction in our work (see Figure 8c–f). If the layer of redox mediators is too high, the electron cannot tunnel, and all currents are diminished. However, the absorption observed in UV–vis spectroscopy remains high because of the low HOMO–LUMO gap of each quinone unit of PDA. This model is also in agreement with recently published computational work by Matta et al., who showed localized dipole moments across the PDA octamers included by catechol/quinone pairs, leading to the entrapment of electrons and holes.[66]

Finally, high-voltage sine-amplitude (500 mV) NL-EIS spectra were collected for TNT|PDA samples with different PDA thicknesses (Figure 10g–i). In the case of pure TNTs, there is a huge semicircle, and the charge-transfer resistance is equal to 10 kΩ cm^2. This behavior is because only the reduction of ferrocyanides can occur on this material. However, for the 5-cycled, 10-cycled, and 25-cycled TNT|PDA samples, the semicircles are smaller and there is a tremendous decrease in the charge-transfer resistance down to ca. 0.5 kΩ cm^2 (Table S2). Moreover, in the case of the 50-cycled sample, both the size of the semicircle and R_{ct} increase once again. These observations support the previously introduced idea that smaller thicknesses of PDA (5 nm) facilitate charge transfer, while bigger thicknesses (8 nm) quench the charge transfer.

In contrast to the R_{ct} variations, the Q values of the CPE elements remain constant regardless of the sinus amplitude. In other words, the structure of the double layer does not contain significant electrical nonlinearities. It should be acknowledged that the quality of the fit in the low-frequency region is getting poorer, which is typical behavior in nonlinear EIS experiments.[64] In summary, there are several pieces of evidence suggesting the semimetallic character of the designed TNT|PDA junctions. The presence of both oxidation and reduction peaks on the CV curves for ferrocyanide electrochemistry was observed, while TiO_2 is an n-type semiconductor and should exhibit only a reduction peak. The missing flat-band potential and potential-dependent capacitance were registered during the Mott–Schottky analysis. The double layer is the only source of the capacitance and space charge region characteristic for semiconductors that was not observed or was negligible. We recorded additional absorption bands on optical spectroscopy in the visible range analogously to those observed in plasmonic metallic nanoparticles.[67] Furthermore, an additional band revealed on the IPCE action map in the visible range strongly suggests the presence of midgap states capable of both electronic excitation and separation of excitons.[68] However, the electric

https://doi.org/10.1021/acs.jpcc.2c08804
J. Phys. Chem. C 2023, 127, 12662–12677

field required for the separation was not induced in the space charge layer but rather by the intermolecular interactions. Lastly, the conducted DFT calculations of the TiO_2—PDA interfaces supported the concept of occupied midgap states since the Fermi level crosses those states located at the bottom of the conduction band similarly as it crosses the occupied band in the case of metals. It is worth noting that the semimetallic properties of PDA within the TNT-PDA composite could be confirmed through measurements of its electrical characteristics at varying temperatures. However, due to the temperature sensitivity of the synthesized PDA and its thermal decomposition at 175 °C, it was impossible to construct an effective Arrhenius plot (refer to Figure S14 in the Supporting Information file). Ultraviolet photoelectron spectroscopy (UPS) is another possible complementary technique to investigate the semimetallicity issue. However, this method requires high vacuum conditions that could potentially alter the morphology of the entire structure, including both the PDA coating and the nanotubes underneath. Furthermore, while PDA is stable when exposed to near-UV light, which is relevant for photoelectrochemical applications, it remains uncertain whether far-UV light would maintain the surface chemistry. As a result, the use of UPS for the TNT-PDA material under investigation is debatable.

4. CONCLUSIONS

In this work, PDA was deposited uniformly on the surface of hydrogenated TNTs through potentiodynamic electropolymerization. The chemical structure of the resulting PDA layer and its adsorption geometry on the surface of TiO_2 at both molecular and micrometer scales are highly dependent on the pH used for the electropolymerization. Several structure−property relationships were established:

- After PDA modification, a set of localized midgap states are introduced into the DOS spectrum of TiO_2 and a significant portion of these states is occupied, leading to the semimetallic properties of the TNT|DPA junctions.
- XPS studies and DFT analyses indicate that the alkaline-based PDA exhibits more conjugated quinone units with a lower HOMO−LUMO gap than catecholic units compared to acid-based PDA, leading to higher absorption in the visible range.
- Up to a 20× increase in the photocurrent response of TNTs is observed, and the IPCE maps indicate that the enhancement occurs mainly in the visible range.
- Electrochemical investigations of the TNT|PDA junctions also suggest the semimetallic character of the material because both oxidation and reduction peaks are present on the ferrocyanide voltammograms, and the Mott−Schottky plot does not exhibit the flat-band potential.

The study proposes a cheap and facile strategy for photosensitization of metal oxide semiconductors with PDA. On top of that, both experimental and theoretical results strongly suggest the semimetallic character of the modified material in which PDA serves as a set of surface-distributed redox mediators rather than a semiconductive polymer. This viewpoint opens up a new perspective for understanding the general properties of polymer semiconductor junctions instead of the standard picture of the p−n junction. Consequently, in the long term, this perspective might be helpful in improving the performance of various photoelectrochemical devices.

■ ASSOCIATED CONTENT

Supporting Information

The Supporting Information is available free of charge at https://pubs.acs.org/doi/10.1021/acs.jpcc.2c08804.

Quantitative analysis of the XPS data of TNT_PDA samples; EIS equivalent circuit parameters obtained from fitting the spectra presented in Figure 9; additional SEM images with different magnifications and areas on the sample; Raman maps and data elucidating the issue of PDA uniformity; transient photocurrents of four different TNT_b-PDA samples using monochromatic illumination; data connected to the issue of PDA stability, including SEM, XPS, FT-IR, optical, and FT-IR measurements of TNT_PDA before and after exposure to UV light; and two-point probe measurements of the TNT-bPDA electrical properties (PDF)

■ AUTHOR INFORMATION

Corresponding Author

Robert Bogdanowicz − *Department of Metrology and Optoelectronics, Faculty of Electronics, Telecommunications and Informatics, Gdańsk University of Technology, 80-233 Gdańsk, Poland;* orcid.org/0000-0002-7543-2620; Email: rbogdan@eti.pg.edu.pl

Authors

Adrian Olejnik − *Department of Metrology and Optoelectronics, Faculty of Electronics, Telecommunications and Informatics, Gdańsk University of Technology, 80-233 Gdańsk, Poland; Centre for Plasma and Laser Engineering, The Szewalski Institute of Fluid-Flow Machinery, Polish Academy of Sciences, 80-231 Gdańsk, Poland;* orcid.org/0000-0002-1807-8995

Karol Olbryś − *Faculty of Chemistry, Gdańsk University of Technology, 80-233 Gdańsk, Poland*

Jakub Karczewski − *Institute of Nanotechnology and Materials Engineering and Advanced Materials Center, Gdańsk University of Technology, 80-233 Gdansk, Poland*

Jacek Ryl − *Institute of Nanotechnology and Materials Engineering and Advanced Materials Center, Gdańsk University of Technology, 80-233 Gdansk, Poland;* orcid.org/0000-0002-0247-3851

Katarzyna Siuzdak − *Centre for Plasma and Laser Engineering, The Szewalski Institute of Fluid-Flow Machinery, Polish Academy of Sciences, 80-231 Gdańsk, Poland;* orcid.org/0000-0001-7434-6408

Complete contact information is available at: https://pubs.acs.org/10.1021/acs.jpcc.2c08804

Notes

The authors declare the following competing financial interest(s): Elements of this work are submitted as a patent proposal to the Polish Patent Office #P.442200. No other financial interests or personal relationships are declared.

■ ACKNOWLEDGMENTS

This work was financially supported by the Polish Ministry of Science and Higher Education through Diamentowy grant DI2019 017649. R.B. acknowledges the funding from the National Science Centre, Poland, under the OPUS call in the Weave programme (project number: 2021/43/I/ST7/03205).

REFERENCES

(1) Aguilar-Ferrer, D.; Szewczyk, J.; Coy, E. Recent Developments in Polydopamine-Based Photocatalytic Nanocomposites for Energy Production: Physico-Chemical Properties and Perspectives. *Catal. Today* **2022**, *397*−*399*, 316−349.

(2) Cao, W.; Zhou, X.; McCallum, N. C.; Hu, Z.; Ni, Q. Z.; Kapoor, U.; Heil, C. M.; Cay, K. S.; Zand, T.; Mantanona, A. J.; et al. Unraveling the Structure and Function of Melanin through Synthesis. *J. Am. Chem. Soc.* **2021**, *143*, 2622−2637.

(3) Lee, H. A.; Park, E.; Lee, H. Polydopamine and Its Derivative Surface Chemistry in Material Science: A Focused Review for Studies at KAIST. *Adv. Mater.* **2020**, *32*, 1907505.

(4) Ryu, J. H.; Messersmith, P. B.; Lee, H. Polydopamine Surface Chemistry: A Decade of Discovery. *ACS Appl. Mater. Interfaces* **2018**, *10*, 7523−7540.

(5) Huang, Q.; Chen, J.; Liu, M.; Huang, H.; Zhang, X.; Wei, Y. Polydopamine-Based Functional Materials and Their Applications in Energy, Environmental, and Catalytic Fields: State-of-the-Art Review. *Chem. Eng. J.* **2020**, *387*, 124019.

(6) Liebscher, J.; Mrówczyński, R.; Scheidt, H. A.; Filip, C.; Hădade, N. D.; Turcu, R.; Bende, A.; Beck, S. Structure of Polydopamine: A Never-Ending Story? *Langmuir* **2013**, *29*, 10539−10548.

(7) Abdel-Aziz, A. M.; Hassan, H. H.; Badr, I. H. A. Glassy Carbon Electrode Electromodification in the Presence of Organic Monomers: Electropolymerization versus Activation. *Anal. Chem.* **2020**, *92*, 7947−7954.

(8) d'Ischia, M.; Napolitano, A.; Ball, V.; Chen, C.-T.; Buehler, M. J. Polydopamine and Eumelanin: From Structure−Property Relationships to a Unified Tailoring Strategy. *Acc. Chem. Res.* **2014**, *47*, 3541−3550.

(9) Delparastan, P.; Malollari, K. G.; Lee, H.; Messersmith, P. B. Direct Evidence for the Polymeric Nature of Polydopamine. *Angew. Chem.* **2019**, *131*, 1089−1094.

(10) Hong, S.; Na, Y. S.; Choi, S.; Song, I. T.; Kim, W. Y.; Lee, H. Non-Covalent Self-Assembly and Covalent Polymerization Co-Contribute to Polydopamine Formation. *Adv. Funct. Mater.* **2012**, *22*, 4711−4717.

(11) Della Vecchia, N. F.; Luchini, A.; Napolitano, A.; D'Errico, G.; Vitiello, G.; Szekely, N.; d'Ischia, M.; Paduano, L. Tris Buffer Modulates Polydopamine Growth, Aggregation, and Paramagnetic Properties. *Langmuir* **2014**, *30*, 9811−9818.

(12) Coskun, H.; Aljabour, A.; Uiberlacker, L.; Strobel, M.; Hild, S.; Cobet, C.; Farka, D.; Stadler, P.; Sariciftci, N. S. Chemical Vapor Deposition - Based Synthesis of Conductive Polydopamine Thin-Films. *Thin Solid Films* **2018**, *645*, 320−325.

(13) Jin, Z.; Yang, L.; Shi, S.; Wang, T.; Duan, G.; Liu, X.; Li, Y. Flexible Polydopamine Bioelectronics. *Adv. Funct. Mater.* **2021**, *31*, 2103391.

(14) Yang, L.; Guo, X.; Jin, Z.; Guo, W.; Duan, G.; Liu, X.; Li, Y. Emergence of Melanin-Inspired Supercapacitors. *Nano Today* **2021**, *37*, 101075.

(15) Zou, Y.; Chen, X.; Yang, P.; Liang, G.; Yang, Y.; Gu, Z.; Li, Y. Regulating the Absorption Spectrum of Polydopamine. *Sci. Adv.* **2020**, *6*, No. eabb4696.

(16) Daboss, S.; Lin, J.; Godejohann, M.; Kranz, C. Redox Switchable Polydopamine-Modified AFM-SECM Probes: A Probe for Electrochemical Force Spectroscopy. *Anal. Chem.* **2020**, *92*, 8404−8413.

(17) Almeida, L. C.; Frade, T.; Correia, R. D.; Niu, Y.; Jin, G.; Correia, J. P.; Viana, A. S. Electrosynthesis of Polydopamine-Ethanolamine Films for the Development of Immunosensing Interfaces. *Sci. Rep.* **2021**, *11*, 2237.

(18) Olejnik, A.; Ficek, M.; Szkodo, M.; Stanisławska, A.; Karczewski, J.; Ryl, J.; Dołęga, A.; Siuzdak, K.; Bogdanowicz, R. Tailoring Diffusional Fields in Zwitterion/Dopamine Copolymer Electropolymerized at Carbon Nanowalls for Sensitive Recognition of Neurotransmitters. *ACS Nano* **2022**, *16*, 13183−13198.

(19) Leibl, N.; Duma, L.; Gonzato, C.; Haupt, K. Polydopamine-Based Molecularly Imprinted Thin Films for Electro-Chemical Sensing of Nitro-Explosives in Aqueous Solutions. *Bioelectrochemistry* **2020**, *135*, 107541.

(20) Jastrzebska, M. M.; Isotalo, H.; Paloheimo, J.; Stubb, H. Electrical Conductivity of Synthetic DOPA-Melanin Polymer for Different Hydration States and Temperatures. *J. Biomater. Sci., Polym. Ed.* **1996**, *7*, 577−586.

(21) Mostert, A. B.; Powell, B. J.; Pratt, F. L.; Hanson, G. R.; Sarna, T.; Gentle, I. R.; Meredith, P. Role of Semiconductivity and Ion Transport in the Electrical Conduction of Melanin. *Proc. Natl. Acad. Sci. U.S.A.* **2012**, *109*, 8943−8947.

(22) Corani, A.; Huijser, A.; Gustavsson, T.; Markovitsi, D.; Malmqvist, P.-Å.; Pezzella, A.; d'Ischia, M.; Sundström, V. Superior Photoprotective Motifs and Mechanisms in Eumelanins Uncovered. *J. Am. Chem. Soc.* **2014**, *136*, 11626−11635.

(23) Kim, Y.; Coy, E.; Kim, H.; Mrówczyński, R.; Torruella, P.; Jeong, D.-W.; Choi, K. S.; Jang, J. H.; Song, M. Y.; Jang, D. J.; et al. Efficient Photocatalytic Production of Hydrogen by Exploiting the Polydopamine-Semiconductor Interface. *Appl. Catal., B* **2021**, *280*, 119423.

(24) Dimitrijevic, N. M.; Saponjic, Z. V.; Rabatic, B. M.; Poluektov, O. G.; Rajh, T. Effect of Size and Shape of Nanocrystalline TiO_2 on Photogenerated Charges. An EPR Study. *J. Phys. Chem. C* **2007**, *111*, 14597−14601.

(25) Guan, P.; Bai, H.; Li, C.; Ge, Y.; Xu, D.; Chen, B.; Xia, T.; Fan, W.; Shi, W. Integrated Heterostructure of PDA/Bi-$AgIn_5S_8$/TiO_2 for Photoelectrochemical Hydrogen Production: Understanding the Synergistic Effect of Multilayer Structure. *Adv. Mater. Interfaces* **2018**, *5*, 1701574.

(26) Mao, W.-X.; Lin, X.-J.; Zhang, W.; Chi, Z.-X.; Lyu, R.-W.; Cao, A.-M.; Wan, L.-J. Core−Shell Structured TiO_2@polydopamine for Highly Active Visible-Light Photocatalysis. *Chem. Commun.* **2016**, *52*, 7122−7125.

(27) Wawrzyniak, J.; Grochowska, K.; Karczewski, J.; Kupracz, P.; Ryl, J.; Dołęga, A.; Siuzdak, K. The Geometry of Free-Standing Titania Nanotubes as a Critical Factor Controlling Their Optical and Photoelectrochemical Performance. *Surf. Coat. Technol.* **2020**, *389*, 125628.

(28) Wawrzyniak, J.; Karczewski, J.; Kupracz, P.; Grochowska, K.; Coy, E.; Mazikowski, A.; Ryl, J.; Siuzdak, K. Formation of the Hollow Nanopillar Arrays through the Laser-Induced Transformation of TiO2 Nanotubes. *Sci. Rep.* **2020**, *10*, 20235.

(29) Vargas, W. E.; Niklasson, G. A. Applicability Conditions of the Kubelka−Munk Theory. *Appl. Opt.* **1997**, *36*, 5580.

(30) *Atomistix Toolkit Version 2019.03, Synopsys QuantumWise A/S* (www.quantumwise.com).

(31) Soler, J. M.; Artacho, E.; Gale, J. D.; García, A.; Junquera, J.; Ordejón, P.; Sánchez-Portal, D. The SIESTA Method for *Ab Initio* Order- *N* Materials Simulation. *J. Phys.: Condens. Matter* **2002**, *14*, 2745−2779.

(32) van Setten, M. J.; Giantomassi, M.; Bousquet, E.; Verstraete, M. J.; Hamann, D. R.; Gonze, X.; Rignanese, G.-M. The PseudoDojo: Training and Grading a 85 Element Optimized Norm-Conserving Pseudopotential Table. *Comput. Phys. Commun.* **2018**, *226*, 39−54.

(33) Mayo, S. L.; Olafson, B. D.; Goddard, W. A. DREIDING: A Generic Force Field for Molecular Simulations. *J. Phys. Chem.* **1990**, *94*, 8897−8909.

(34) Ferreira, L. G.; Marques, M.; Teles, L. K. Slater Half-Occupation Technique Revisited: The LDA-1/2 and GGA-1/2 Approaches for Atomic Ionization Energies and Band Gaps in Semiconductors. *AIP Adv.* **2011**, *1*, 032119.

(35) Wawrzyniak, J.; Karczewski, J.; Coy, E.; Iatsunskyi, I.; Ryl, J.; Gazda, M.; Grochowska, K.; Siuzdak, K. Spectacular Oxygen Evolution Reaction Enhancement through Laser Processing of the Nickel-Decorated Titania Nanotubes. *Adv. Mater. Interfaces* **2021**, *8*, 2001420.

(36) Wawrzyniak, J.; Karczewski, J.; Kupracz, P.; Grochowska, K.; Załęski, K.; Pshyk, O.; Coy, E.; Bartmański, M.; Szkodo, M.; Siuzdak, K. Laser-Assisted Modification of Titanium Dioxide Nanotubes in a Tilted Mode as Surface Modification and Patterning Strategy. *Appl. Surf. Sci.* **2020**, *508*, 145143.

(37) Szkoda, M.; Trzciński, K.; Rysz, J.; Gazda, M.; Siuzdak, K.; Lisowska-Oleksiak, A. Electrodes Consisting of PEDOT Modified by

https://doi.org/10.1021/acs.jpcc.2c08804
J. Phys. Chem. C 2023, 127, 12662−12677

Prussian Blue Analogues Deposited onto Titania Nanotubes − Their Highly Improved Capacitance. *Solid State Ionics* **2017**, *302*, 197−201.
(38) Raghunath, P.; Huang, W. F.; Lin, M. C. Quantum Chemical Elucidation of the Mechanism for Hydrogenation of TiO_2 Anatase Crystals. *J. Chem. Phys.* **2013**, *138*, 154705.
(39) Siuzdak, K.; Szkoda, M.; Lisowska-Oleksiak, A.; Karczewski, J.; Ryl, J. Highly Stable Organic−Inorganic Junction Composed of Hydrogenated Titania Nanotubes Infiltrated by a Conducting Polymer. *RSC Adv.* **2016**, *6*, 33101−33110.
(40) Amiri, M.; Amali, E.; Nematollahzadeh, A.; Salehniya, H. Poly-Dopamine Films: Voltammetric Sensor for PH Monitoring. *Sens. Actuators, B* **2016**, *228*, 53−58.
(41) Chalmers, E.; Lee, H.; Zhu, C.; Liu, X. Increasing the Conductivity and Adhesion of Polypyrrole Hydrogels with Electro-polymerized Polydopamine. *Chem. Mater.* **2020**, *32*, 234−244.
(42) Olejnik, A.; Ficek, M.; Siuzdak, K.; Bogdanowicz, R. Multi-Pathway Mechanism of Polydopamine Film Formation at Vertically Aligned Diamondised Boron-Doped Carbon Nanowalls. *Electrochim. Acta* **2022**, *409*, 140000.
(43) Almeida, L. C.; Correia, R. D.; Marta, A.; Squillaci, G.; Morana, A.; La Cara, F.; Correia, J. P.; Viana, A. S. Electrosynthesis of Polydopamine Films - Tailored Matrices for Laccase-Based Biosensors. *Appl. Surf. Sci.* **2019**, *480*, 979−989.
(44) Li, S.; Wang, H.; Young, M.; Xu, F.; Cheng, G.; Cong, H. Properties of Electropolymerized Dopamine and Its Analogues. *Langmuir* **2019**, *35*, 1119−1125.
(45) Wang, J.; Li, B.; Li, Z.; Ren, K.; Jin, L.; Zhang, S.; Chang, H.; Sun, Y.; Ji, J. Electropolymerization of Dopamine for Surface Modification of Complex-Shaped Cardiovascular Stents. *Biomaterials* **2014**, *35*, 7679−7689.
(46) Klosterman, L.; Ahmad, Z.; Viswanathan, V.; Bettinger, C. J. Synthesis and Measurement of Cohesive Mechanics in Polydopamine Nanomembranes. *Adv. Mater. Interfaces* **2017**, *4*, 1700041.
(47) Loget, G.; Yoo, J. E.; Mazare, A.; Wang, L.; Schmuki, P. Highly Controlled Coating of a Biomimetic Polymer in TiO2 Nanotubes. 2016, arXiv:1610.04184. https://doi.org/10.48550/ARXIV.1610.04184.
(48) Guo, Z.; Wang, G.; Fu, H.; Wang, P.; Liao, J.; Wang, A. Photocatalytic Degradation of Methylene Blue by a Cocatalytic PDA/TiO_2 Electrode Produced by Photoelectric Polymerization. *RSC Adv.* **2020**, *10*, 26133−26141.
(49) Kupracz, P.; Grochowska, K.; Karczewski, J.; Wawrzyniak, J.; Siuzdak, K. The Effect of Laser Re-Solidification on Microstructure and Photo-Electrochemical Properties of Fe-Decorated TiO2 Nanotubes. *Materials* **2020**, *13*, 4019.
(50) Haryński, Ł.; Grochowska, K.; Karczewski, J.; Ryl, J.; Rysz, J.; Siuzdak, K. Free-Standing TiO_2 Nanotubes Decorated with Spherical Nickel Nanoparticles as a Cost-Efficient Electrocatalyst for Oxygen Evolution Reaction. *RSC Adv.* **2021**, *11*, 219−228.
(51) Tesler, A. B.; Altomare, M.; Schmuki, P. Morphology and Optical Properties of Highly Ordered TiO_2 Nanotubes Grown in NH_4F/*o*-H_3PO_4 Electrolytes in View of Light-Harvesting and Catalytic Applications. *ACS Appl. Nano Mater.* **2020**, *3*, 10646−10658.
(52) Chiarello, G. L.; Zuliani, A.; Ceresoli, D.; Martinazzo, R.; Selli, E. Exploiting the Photonic Crystal Properties of TiO_2 Nanotube Arrays To Enhance Photocatalytic Hydrogen Production. *ACS Catal.* **2016**, *6*, 1345−1353.
(53) Sun, X.; Yan, L.; Xu, R.; Xu, M.; Zhu, Y. Surface Modification of TiO2 with Polydopamine and Its Effect on Photocatalytic Degradation Mechanism. *Colloids Surf., A* **2019**, *570*, 199−209.
(54) Wang, Q.; Jia, F.; Song, S.; Li, Y. Hydrophilic MoS2/Polydopamine (PDA) Nanocomposites as the Electrode for Enhanced Capacitive Deionization. *Sep. Purif. Technol.* **2020**, *236*, 116298.
(55) Gelderman, K.; Lee, L.; Donne, S. W. Flat-Band Potential of a Semiconductor: Using the Mott−Schottky Equation. *J. Chem. Educ.* **2007**, *84*, 685.
(56) Kim, H.; Kim, G. Adsorption Properties of Dopamine Derivatives Using Carbon Nanotubes: A First-Principles Study. *Appl. Surf. Sci.* **2020**, *501*, 144249.
(57) Ambrico, M.; Vecchia, N. F. D.; Ambrico, P. F.; Cardone, A.; Cicco, S. R.; Ligonzo, T.; Avolio, R.; Napolitano, A.; d'Ischia, M. A Photoresponsive Red-Hair-Inspired Polydopamine-Based Copolymer for Hybrid Photocapacitive Sensors. *Adv. Funct. Mater.* **2014**, *24*, 7161−7172.
(58) Li, H.; Marshall, T.; Aulin, Y. V.; Thenuwara, A. C.; Zhao, Y.; Borguet, E.; Strongin, D. R.; Ren, F. Structural Evolution and Electrical Properties of Metal Ion-Containing Polydopamine. *J. Mater. Sci.* **2019**, *54*, 6393−6400.
(59) Kund, J.; Daboss, S.; D'Alvise, T. M.; Harvey, S.; Synatschke, C. V.; Weil, T.; Kranz, C. Physicochemical and Electrochemical Characterization of Electropolymerized Polydopamine Films: Influence of the Deposition Process. *Nanomaterials* **2021**, *11*, 1964.
(60) Yang, P.; Zhang, S.; Chen, X.; Liu, X.; Wang, Z.; Li, Y. Recent Developments in Polydopamine Fluorescent Nanomaterials. *Mater. Horiz.* **2020**, *7*, 746−761.
(61) Bard, A. J.; Faulkner, L. R. *Electrochemical Methods: Fundamentals and Applications*, 2nd ed.; Wiley: New York, 2001.
(62) Song, J.; Liu, H.; Lei, M.; Tan, H.; Chen, Z.; Antoshin, A.; Payne, G. F.; Qu, X.; Liu, C. Redox-Channeling Polydopamine-Ferrocene (PDA-Fc) Coating To Confer Context-Dependent and Photothermal Antimicrobial Activities. *ACS Appl. Mater. Interfaces* **2020**, *12*, 8915−8928.
(63) Kanyong, P.; Rawlinson, S.; Davis, J. Fabrication and Electrochemical Characterization of Polydopamine Redox Polymer Modified Screen-Printed Carbon Electrode for the Detection of Guanine. *Sens. Actuators, B* **2016**, *233*, 528−534.
(64) Fasmin, F.; Srinivasan, R. Review—Nonlinear Electrochemical Impedance Spectroscopy. *J. Electrochem. Soc.* **2017**, *164*, H443−H455.
(65) Bondarenko, A. S.; Ragoisha, G. A. *Progress in Chemometrics Research*; Pomerantsev, A. L., Ed.; Nova Science Publishers: New York, 2005; pp 89−102. the program is available online at. http://www.abc.chemistry.bsu.by/vi/Analyser/.
(66) Matta, M.; Pezzella, A.; Troisi, A. Relation between Local Structure, Electric Dipole, and Charge Carrier Dynamics in DHICA Melanin: A Model for Biocompatible Semiconductors. *J. Phys. Chem. Lett.* **2020**, *11*, 1045−1051.
(67) Boken, J.; Khurana, P.; Thatai, S.; Kumar, D.; Prasad, S. Plasmonic Nanoparticles and Their Analytical Applications: A Review. *Appl. Spectrosc. Rev.* **2017**, *52*, 774−820.
(68) Liu, B.; Zhao, X.; Yu, J.; Parkin, I. P.; Fujishima, A.; Nakata, K. Intrinsic Intermediate Gap States of TiO2 Materials and Their Roles in Charge Carrier Kinetics. *J. Photochem. Photobiol., C* **2019**, *39*, 1−57.